Astronomy & Astrophysics manuscript no. halo_model_cib
June 1, 2022

A simple halo model formalism for the cosmic infrared background and its correlation with the thermal Sunyaev Zel'dovich effect

A. Maniyar[1,2], M. Béthermin[1], and G. Lagache[1]

[1]Aix Marseille Univ, CNRS, CNES, LAM, Marseille, France
[2]Center for Cosmology and Particle Physics, Department of Physics, New York University, New York, NY, 10003, USA
e-mail: abhishek.maniyar@nyu.edu

Received xx; accepted xx;

ABSTRACT

Modelling the anisotropies in the cosmic infrared background (CIB) on all the scales is a challenging task due to the complex nature of the galaxy evolution and thus often requires too many parameters in order to fit the observational data. In this paper, we present a new halo model for the anisotropies of the CIB using only four parameters. Our model connects the mass accretion on the dark matter halos to the star formation rate. Despite its relative simplicity, it is able to fit both the *Planck* and *Herschel* CIB power spectra and is consistent with the external constraints for the obscured star formation history derived from infrared deep surveys used as priors for the fit. Using this model, we find that the halo mass with the maximum efficiency for converting the accreted baryons into stars is $\log_{10} M_{\rm max} = 12.94^{+0.02}_{-0.02}\ M_{\odot}$, consistent with other studies. Accounting for the mass loss through stellar evolution, we find, for an intermediate age galaxy, that the star formation efficiency defined as $M_{\star}(z)/M_{b}(z)$ is equal to 0.19 and 0.21 at redshift 0.1 and 2 respectively, in good agreement with the values obtained by previous studies. It is the first time that a CIB model is used to fit *Planck* and *Herschel* CIB power spectra simultaneously. The high angular resolution of *Herschel* allows us to go on very small scales making it possible to constrain the shot noise and the 1-halo term separately which is difficult to do using the *Planck* data alone. However we find that the large angular scale *Planck* and *Herschel* data are not fully compatible with the small scale Herschel data (for $\ell > 3000$). The CIB is expected to be correlated with the thermal Sunyaev Zel'dovic (tSZ) signal of galaxy clusters. Using this halo model for the CIB, and a halo model for the tSZ with a single parameter we also provide a consistent framework to calculate the CIB×tSZ cross-correlation, which requires no extra parameter. To certain extent, the CIB at high frequencies traces galaxies at low redshifts which reside in the clusters contributing to the tSZ giving rise to the 1-halo term of this correlation while the 2-halo term comes from the overlap in the redshift distribution of the tSZ clusters and CIB galaxies. The CIB×tSZ correlation is thus found to be higher when inferred with a combination of two widely spaced frequency channels (e.g. 143x857 GHz). We also find that even at $\ell \sim 2000$, the 2-halo term of this correlation is still comparable to the 1-halo term and has to be accounted for in the total cross-correlation. The CIB, tSZ, and CIB×tSZ act as foregrounds while measuring the kinetic SZ (kSZ) power spectrum from the cosmic microwave background power spectrum and need to be removed. Due to its simplistic nature and low number of parameters, the halo model formalism presented here for these foregrounds is quite useful for such an analysis to measure the kSZ power spectrum accurately.

Key words. Infrared: diffuse background - cosmic background radiation - Submillimeter: galaxies - Galaxies: clusters: general - Cosmology: observations - Methods: data analysis.

1. Introduction

The cosmic infrared background (CIB) is made up of the cumulative emission of the infrared radiation from the dusty star forming galaxies throughout the Universe. It traces the star formation history of the Universe spanning a wide range of redshift $0 \leq z \sim 6$. Measurements of the CIB can thus be used as a powerful tool to map the star formation at high redshifts (Knox et al., 2001). Although the CIB was first detected by Puget et al. (1996), Lagache & Puget (2000) and Matsuhara et al. (2000) were the first ones to detect and discuss the anisotropies in the CIB that are due to unresolved extra-galactic sources. There are correlated anisotropies in the CIB which are excellent probes of the large scale structure of the Universe (e.g. Hanson et al., 2013). These were first discovered by *Spitzer* (Lagache et al., 2007) and then were subsequently accurately measured by Planck and Herschel (Planck Collaboration et al., 2014c, Viero et al., 2013a). These anisotropies in the CIB are excellent tracers of the large scale structure of the Universe.
Another such tracers of the underlying dark matter distribution are massive galaxy clusters. Hot electrons in these galaxy clusters Compton scatter the CMB photons and give rise to the so called thermal Sunyaev Zel'dovich (tSZ) effect. A part of the CIB is sourced by the dusty star forming galaxies residing in the galaxy clusters. Thus, the tSZ and the CIB are expected to be correlated to certain extent. This correlation has indeed been indirectly measured and shown to be positive by Reichardt et al. (2012), Dunkley et al. (2013), and George et al. (2015) and thus has to be considered in the CMB power spectrum data analysis. Planck Collaboration et al. (2016c) also reported a measurement of the cross-correlation between the tSZ and CIB using the *Planck* data. In order to model the CIB×tSZ signal, we in turn need accurate models of the CIB anisotropies and the tSZ.
On the large angular scales, we can use the fact that the clustering of the CIB traces the large scale distribution of the matter in the Universe up to some bias factor. This makes modelling the CIB anisotropies on the large angular scales quite straightforward as done in (e.g. Planck Collaboration et al., 2014c, Maniyar et al., 2018). However, in order to describe the anisotropies on both the large and small angular scales

coherently, a 'halo model' approach as developed by Cooray & Sheth (2002) is generally used. With the assumption inside the halo model that all the galaxies reside in the dark matter haloes, the clustering can be considered as the sum of two components: 1-halo term (P_{1h}) which takes into account the small scale clustering due to the correlations between the galaxies within the same halo; and 2-halo term (P_{2h}) which accounts for the clustering on large scales due to the correlations between galaxies in different halos. Along with the assumption that all the dark matter lies within the collapsed and symmetric haloes, four ingredients are required to characterize the galaxy power spectrum within the halo modelling context: number density of the halos per unit mass given by the halo mass function; the halo bias between the haloes and the dark matter; spatial distribution of the dark matter inside a halo given by the halo density profile; and halo occupation distribution (HOD) which is a prescription for filling up the dark matter halos with galaxies.

The first generation of the models built to interpret the CIB anisotropies were based on either a HOD model or a combination of models of emissivities of the IR galaxies and a linear bias (Knox et al., 2001, Lagache et al., 2007, Amblard & Cooray, 2007, Viero et al., 2009, Planck Collaboration et al., 2011, Amblard et al., 2011, Xia et al., 2012). These approaches assumed that the emissivity density is traced by the galaxy number density implying that all galaxies contribute equally to the emissivity irrespective of their host halo masses. It would mean that all the galaxies have the same luminosity. However, as has been pointed out by Shang et al. (2012), both the luminosity and clustering of the galaxies are closely related to the host halo mass. In general, galaxies situated in more massive halos are more luminous as a result of more stellar mass and are also more clustered. A lack of accounting for this effect can lead to an interpretation of the clustering signal on smaller angular scales as being due to very high number of satellite haloes (which was the case for Amblard et al. 2011) than what is found in numerical simulations (discussion in Viero et al. 2013b).

Subsequently several studies such as Shang et al. (2012), Viero et al. (2013b), Planck Collaboration et al. (2014c) etc. have improved upon the previous halo models by considering a link between the galaxy luminosity (L) and the host halo mass (M_h) in their model (through a $L - M_h$ relation). Although their approach is able to fit the CIB power spectra, their description of the IR galaxies is quite simple (e.g. a single SED for all galaxy types but with evolving dust temperature or no scatter on the $L - M_h$ relation). These models are useful to derive quantities like the halo mass for the most efficient star formation, but it is hard to test their validity because a good fit can be obtained easily given with the high number of free parameters in these models. Also, without considering any priors, the predictions of these models for physical quantities like SFRD do not match with the corresponding constraints from the linear model or galaxy surveys (e.g. Planck Collaboration et al., 2014c). This shows the need for physically motivated models which apart from the power spectra, can provide a good fit/prediction for other physical quantities like the SFRD. Béthermin et al. (2013) used a semi-empirical model based on the observed relation between the stellar mass M_* and the star formation rate (SFR) which they linked to the corresponding halo mass using abundance matching. This models gives CIB power spectra consistent with the measurements. In the present paper, inspired by their findings of the SFR/BAR relation with respect to the halo mass (where BAR represents the baryonic accretion rate), we develop a simpler halo model for the CIB anisotropies with just four parameters. Our model connects the mass accretion on the dark matter halos to the corresponding star formation rate.

As for the tSZ, it is measured through the so called Compton parameter (y; Sec. 4). The Planck Collaboration provided an all-sky map of this Compton y parameter as well as an estimate of the tSZ angular power spectrum up to $\ell \approx 1300$ (Planck Collaboration et al., 2014a, 2016d). Bolliet et al. (2018) used these data to constrain the cosmological parameters (equation of state of the dark energy w particularly) along with the tSZ parameter. Here, we use this halo model of the tSZ to calculate the tSZ power spectra.

Addison et al. (2012) calculated the CIB-tSZ correlation within the halo model framework. They first present a formalism to calculate this correlation using a CIB halo model which does not account for the dependence of the source flux on the halo mass, and then expand their formalism to account for this effect. However, the CIB halo model they finally consider (from Xia et al. (2012)) to calculate the CIB-tSZ correlation does not account for the aforementioned $L - M_h$ dependency. Here, we present a halo model formalism to calculate the CIB×tSZ cross-correlation using our new halo model for the CIB and the halo model for the tSZ from Bolliet et al. (2018).

This paper is structured as follows. We begin in Sect. 2 by presenting our halo model for the CIB anisotropies and subsequently present the CIBxCMB lensing correlation within this framework. Sect. 3 then presents the constraints on the CIB model parameters through the data and corresponding results. In Sect. 4 we provide the halo model for the tSZ. Finally, in Sect. 5 we present the halo model formalism for the CIB×tSZ correlation as well as the predictions for its power spectra and angular scale dependance[1]. Conclusions are given in Sect. 6. In the end App. A, B, and C provide details about the CIB halo model formalism as well as the comparison between the Planck and Herschel CIB power spectrum data.

Wherever required, we used a Chabrier mass function (Chabrier, 2003) and the Planck 2015 flat ΛCDM cosmology (Planck Collaboration et al., 2016b) with $\Omega_m = 0.33$ and $H_0 = 67.47\,\mathrm{km\,s^{-1}\,Mpc^{-1}}$.

2. A new halo model for the CIB power spectrum

The starting point for our model is the accretion of matter on the dark matter halos. We then connect the accretion of the baryonic gas on the dark matter halos to the star formation rate (SFR) corresponding to these halos. The SFR is defined separately for the central and satellite galaxies in a halo. Using the SFR from a given halo, we then calculate the emissivity of all the halos of mass M_h at a given redshift which then is used to calculate the angular power spectrum of the CIB anisotropies.

The angular power spectrum of the CIB anisotropies is defined as

$$\left\langle \delta I^{\nu}_{\ell m} \delta I^{\nu'}_{\ell' m'} \right\rangle = C_{\ell}^{\nu\times\nu'} \times \delta_{\ell\ell'}\delta_{mm'}\,, \tag{1}$$

where ν is the frequency of the observation and I_ν is the intensity of the CIB measured at that frequency. The intensity is a function of the comoving emissivity j through

$$\begin{aligned} I_\nu &= \int \frac{d\chi}{dz} a\, j(\nu, z) dz \\ &= \int \frac{d\chi}{dz} a\, \bar{j}(\nu, z)\Big(1 + \frac{\delta j(\nu, z)}{\bar{j}(\nu, z)}\Big) dz\,, \end{aligned} \tag{2}$$

[1] Code to calculate the CIB, tSZ, and CIB×tSZ power spectra is made available online at `https://github.com/abhimaniyar/halomodel_cib_tsz_cibxtsz`

where $\chi(z)$ is the comoving distance to redshift z, and $a = 1/(1+z)$ is the scale factor of the Universe, and $\delta j(\nu, z)$ are the emissivity fluctuations of the CIB. We expand the Eq. 2 this way between the mean value and its fluctuations because as we can see from Eq. 1, the power spectrum is calculated using the fluctuations around the mean value. Thus, combining Eqs. 1 and 2, and using the Limber's approximation (Limber, 1954) for the flat sky which helps us avoid the spherical Bessel function calculations and makes the computation easier, we get

$$C_\ell^{\nu\times\nu'} = \int \frac{dz}{\chi^2}\frac{d\chi}{dz} a^2 \bar{j}(\nu, z)\bar{j}(\nu', z) P_j^{\nu\times\nu'}(k = \ell/\chi, z)\,, \qquad (3)$$

where at a given redshift, $P_j^{\nu\times\nu'}$ is the 3D power spectrum of the emissivity and is defined as

$$\left\langle \delta j(k,\nu)\delta j(k',\nu')\right\rangle = (2\pi)^3 \bar{j}(\nu)\bar{j}(\nu') P_j^{\nu\times\nu'}(k)\delta^3(k-k')\,, \qquad (4)$$

Thus we have to calculate δj to obtain the CIB angular power spectrum. For this purpose we connect (Sec. 2.3) the SFR of the halos with the specific emissivity $\frac{dj_\nu}{d\log M_h}(M_h, z)$ and integrate it over all the halo masses and redshift range to obtain the CIB power spectra.

2.1. From accretion on the dark matter halos to SFR

The dark matter halos grow in mass over time through diffuse accretion and mergers with other lower mass halos (e.g. Fakhouri et al., 2010). These are also responsible for the growth of stellar mass in galaxies through galaxy-galaxy mergers and through accretion of the gas. The baryonic gas accreted by a given dark matter halo would form stars depending upon certain factors. This is the starting point of our model. As we mentioned earlier, previous studies utilised a parametric $L - M_h$ relation to get the power spectra. Instead of assuming a $L - M_h$ relation with an evolution in redshift, we connect the above-said accretion rate on a dark matter halo with the corresponding star formation rate. This gives us a SFR$-M_h$ relation which is, in substance, similar to a $L - M_h$ relation, with the difference between our approach and the others being a more physical starting point of the parameterization.

There is a physical motivation behind this approach. This link between the accreted baryons and SFR is quite natural. The stars form out of the gas reservoirs contained within their host galaxies residing in the dark matter halos. The amount of the gas present at a given time depends upon the amount of the gas accreted by the host dark matter halo. We are assuming here that this accreted gas gets converted into stars with an efficiency which is a function of the mass of the halo and redshift. We use a lognormal parameterization between the halo mass and the ratio of the SFR and the baryonic accretion rate BAR for a halo (i.e. SFR/BAR)

$$\frac{\mathrm{SFR}}{\mathrm{BAR}}(M_h, z) = \eta = \eta_{\max}\, e^{-\frac{(\log M_h - \log M_{\max})^2}{2\sigma^2_{M_h}(z)}} \qquad (5)$$

where M_h is the halo mass, $M_{\max}$ represents the mass with the highest star formation efficiency $\eta_{\max}$ and $\sigma_{M_h}(z)$ is the variance of the lognormal which here represents the range of masses over which the star formation is efficient. The ratio SFR/BAR represents the efficiency (η) of the dark matter halo of a given mass (M_h) at a redshift (z) to convert the accreted baryonic mass into stars.

The choice of the lognormal shape is quite logical. Several studies (e.g. Viero et al., 2013a, Planck Collaboration et al., 2014c, Maniyar et al., 2018) have found that the dark matter halos within the mass range $10^{12} - 10^{13} M_\odot$ form the stars most efficiently. With an empirical model, Béthermin et al. (2013) show in their Fig. 17 that the star formation efficiency as a function of instantaneous halo mass is the highest in the halos with masses $\sim 10^{12} M_\odot$ which does not change considerably over a range of redshifts whereas, the efficiency falls off drastically on the masses above and below the most efficient mass. This effect can be understood physically. Below the mass of the highest efficiency of the star formation, the gravitational potential of the dark matter halo is lower and the supernovae feedback is strong enough to remove the gas from the galaxy (e.g. Silk, 2003) and thereby decreasing the star formation. On the other side of the spectrum, at higher masses, the cooling time of the gas becomes much longer than the free fall time (e.g. Kereš et al., 2005). This suppression of the isotropic cooling of the gas could be due to the energy injection in the halo atmosphere by active galactic nuclei (AGN) which in turn suppresses the star formation (e.g. Somerville et al., 2008). Therefore, we here assume a lognormal shape for the efficiency of SFR whereby the star formation is highest for halo mass $M_{\max}$ with a significant contribution to the SFR coming from a range of masses around $M_{\max}$ driven by σ_{M_h} and falls off considerably on very high and very low masses.

For a given halo mass at a given redshift the BAR is given as

$$\mathrm{BAR}(M_h, z) = \langle \dot{M}(M_h, z)\rangle \times \Omega_b(z)/\Omega_m(z)\,, \qquad (6)$$

where Ω_b and Ω_m are the dimensionless cosmological baryonic density and total matter density respectively (thus, ratio of the two gives the baryonic matter fraction at a given redshift which is in fact constant with redshift as they have the same evolution with redshift). $\dot{M}(M_h, z)$ is the mass growth rate. Fakhouri et al. (2010) provide the mean and median mass growth rates of halos of mass M_h at redshift z. We use the mean mass growth rate given as

$$\langle \dot{M}\rangle_{\mathrm{mean}} = 46.1\ M_\odot\ \mathrm{yr}^{-1}\left(\frac{M_h}{10^{12} M_\odot}\right)^{1.1} \times (1 + 1.11z)\sqrt{\Omega_m(1+z)^3 + \Omega_\Lambda} \qquad (7)$$

It has to be noted that this approach presumes there is no 'gas reservoir effect' i.e. the accreted gas is immediately converted into stars and it is not collected over time forming reservoirs in (Daddi et al., 2010) and around galaxies (Cantalupo et al., 2012). It has been shown that (e.g. Saintonge et al., 2013, Béthermin et al., 2015, Dessauges-Zavadsky et al., 2015) the depletion timescale which is the ratio of the mass of the molecular gas to the SFR ranges from $\sim 0.5 - 1$ Gyr, which is much smaller than the typical galaxy evolution timescales (several Gyr). Thus, the gas reservoir effect is not expected to affect the results over the long timescale which is being considered here. Along the same lines, it is also assumed that there is no recycled gas (i.e. the gas expelled by the supernovae) contributing to the star formation (semi-analytical models of e.g. Cousin et al. (2015, 2019) show that feedback from supernovae can play a part in regulating star formation). In spite of these assumptions, we will see that this simple physical model gives a good description of the CIB power spectra.

In our model, we consider the maximum efficiency $\eta_{\max}$ and mass of maximum efficiency $M_{\max}$ to be independent of redshift i.e. they do not evolve with redshift. However, we let σ_{M_h} evolve with redshift. The motivation to let σ_{M_h} evolve with redshift is to accommodate the star formation from massive halos

at higher redshifts and reduce at lower redshifts. It has been observed (Popesso et al., 2015) that at lower redshifts ($z \leq 1.5-2$), star formation is quite inefficient in massive halos (typical galaxy cluster environments) i.e. at low redshifts massive halos contain mostly passive galaxies. On the contrary, it has been shown that at high redshift massive galaxies (often residing in the proto-clusters i.e. the progenitors of the clusters at redshift zero) can have efficient star formation (e.g. Miller et al. 2018, Wang et al. 2018).
Thus we let σ_{M_h} evolve with redshift as

$$\sigma_{M_h}(z) = \sigma_{M_{h0}} - \tau \times \max(0, z_c - z) \tag{8}$$

where z_c is a redshift below which σ_{M_h} evolves with redshift and $\sigma_{M_{h0}}$ is the value of σ_{M_h} above z_c, and τ is the parameter driving this evolution with redshift (τ here should not be confused with the optical depth parameter from the CMB analysis). It has to be noted that following the reasoning mentioned before, this evolution is applied only for halos with masses greater than the mass of maximum efficiency $M_{\rm max}$ and below redshift z_c i.e. the parameterization is not a symmetrical lognormal below redshift z_c. The width of the lognormal is smaller on the side of the curve with halos heavier than $M_{\rm max}$ below redshift z_c. However, above redshift z_c, the parameterization is a symmetrical lognormal with no evolution in the width of the lognormal $\sigma_{M_{h0}}$. We fix $z_c = 1.5$. Other values for z_c were tried which more or less gave the same results, but the model with $z_c = 1.5$ provided the best fit for the SFRD history.

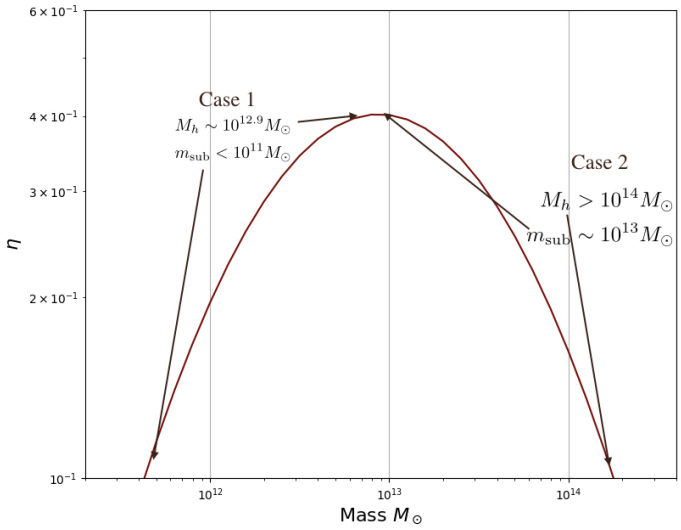

Fig. 1. Lognormal parameterization (Eq. 5) between the halo mass ($M_\odot$) and ratio between the SFR and the baryonic accretion rate, η. We show two extreme cases with halos near the peak of efficiency containing subhalos with very small mass (case 1), and very massive halos containing subhalos near the peak of efficiency (case 2). Using the same recipe to calculate the satellite galaxy SFR in these two cases might result in unphysical values within the assumptions of our model and therefore we suggest two different ways to calculate the SFR for satellite galaxies (Sec. 2.2).

2.2. SFR for the halos and subhalos

For a given value of the halo mass and redshift, we can calculate η using Eq. 5 and multiply it by the corresponding BAR calculated using Eq. 6 to obtain the SFR i.e.

$$\mathrm{SFR}(M_h, z) = \eta(M_h, z) \times \mathrm{BAR}(M_h, z)\,. \tag{9}$$

This is the procedure to obtain the SFR for the halos. There is a slight modification while calculating the SFR for the subhalos residing within these halos. We first of all assume that for a given halo with mass M_h, the subhalo masses ($m_{\rm sub}$) range from $M_{\rm min}$ to M_h. In this analysis, we fix $M_{\rm min} = 10^5 M_\odot$. Changing the minimum mass between $10^4 M_\odot$ and $10^8 M_\odot$ makes negligible change in the calculation of the power spectra. The SFR for the subhalos can be calculated in two ways. The first way is the approach similar to the one for the halos which is calculating the efficiency η and then multiplying with the BAR value to obtain the SFR i.e. replacing M_h by $m_{\rm sub}$ in Eq. 9. This assumes the same lognormal parameterization of η for subhalos as that of the central halos. The other way to calculate the SFR in subhalos is

$$\mathrm{SFR}_{\rm sub} = \mathrm{SFR}_c \times \frac{m_{\rm sub}}{M_h} \tag{10}$$

i.e. SFR for the subhalo is obtained by weighing the halo SFR (SFR_c) by the subhalo to halo mass ratio. For every subhalo of a given halo, we calculate the SFR with both these approaches and take the smaller of the two as a representative of the SFR for the subhalo.

The reasoning behind this can be understood using Fig. 1. Let us first consider Case 1 from the figure. In this case, the main halo has a mass ($\sim 10^{12.9} M_\odot$) very near to the peak of efficiency of star formation (for these particular choice of parameters for the lognormal) i.e. the central galaxy is forming stars very efficiently (see Eq. 9). This halo will have subhalos ranging from $10^5 M_\odot - 10^{12.9} M_\odot$. Let us take the case of a subhalo with mass $< 10^{11} M_\odot$. As was pointed out before, the subhalos with very low mass have low gravitational potential and it is hard for them to hold onto the gas inside against the pressure from e.g. supernova feedback. Thus, they are expected to have low star formation. This is satisfied in case 1 as we can see that at lower masses, the efficiency is indeed very small and they are not expected to have a significant contribution to the total SFR of the halo. Thus in this case, the SFR for the subhalos can directly be computed by substituting the halo mass (M_h) by subhalo mass ($m_{\rm sub}$) in Eq. 9. As an example, for a subhalo of mass $10^{11} M_\odot$ belonging to a central halo of mass $10^{12.9} M_\odot$, the SFR calculated using Eq. 9 comes out to be 2% of the value that we get for the SFR obtained using Eq. 10 and thus we take former as the value for the SFR.
Now let us consider the second case. Here, the main halo is quite massive ($> 10^{14} M_\odot$) and far away from the peak of efficiency. Thus, it does not have a lot of star formation. However, in this case this halo can contain a subhalo with a mass around the peak of the efficiency ($\sim 10^{12.9} M_\odot$). Going by Eq. 9, substituting M_h by $m_{\rm sub}$ this subhalo will have a significant amount of star formation. Again, as pointed out earlier, the gas inside massive halos is quite hot and there are mechanisms at play (e.g. X-ray heating, AGN feedback) which suppress the gas cooling and hence make it difficult to form stars. Also, the central massive galaxies in these halos can strip the gas out of the satellite galaxies in the subhalos and thus decreasing the star formation. Thus, these subhalos should not have a significant contribution to the SFR contrary to what we would obtain with Eq. 9. There is an inherent assumption of instantaneous quenching here i.e. the satellite galaxies get quenched at the same time as the central galaxies in a given parent halo. Explicitly avoiding this assumption would need for us to introduce additional quenching parameter as a function of subhalo mass and redshift. This would result in one or two extra parameters being added to the model. However, as we mentioned earlier, our main purpose here is to build a very

simple halo model of the CIB with as less parameters as possible. Thus, in such cases, one way to correct for this is to weight the SFR of the main halo by the mass fraction of the corresponding subhalo i.e. using Eq. 10 to obtain the SFR of the subhalo. The SFR in this case would be smaller than that obtained using Eq. 9 (substituting M_h by $m_{\rm sub}$, of course). Again as an example, for a subhalo of mass $10^{12.9} M_\odot$ belonging to a central halo of mass $10^{14} M_\odot$, the SFR calculated using Eq. 9 comes out to be 2 times larger than the value that we get for the SFR obtained using Eq. 10 at $z = 2$ and thus we take later as the value for the SFR.
Therefore, for every halo we calculate the SFR for the corresponding subhalos using both these methods at every redshift and pick the one with the lower value. This automatically takes care of the extreme cases and helps us avoid adding additional parameters in the model.

2.3. SFR to CIB power spectra

The 1-halo term for power spectrum of the CIB takes into account the clustering of the galaxies within a halo of mass M_h and is calculated as Béthermin et al. (2013) (where $k = \ell/\chi$)

$$C^{1h}_{\ell,\nu,\nu'} = \int\int \frac{d\chi}{dz}\left(\frac{a}{\chi}\right)^2 \Bigg[\frac{dj_{\nu,c}}{d\log M_h}\frac{dj_{\nu',sub}}{d\log M_h}u(k,M_h,z) + \frac{dj_{\nu',c}}{d\log M_h}\frac{dj_{\nu,sub}}{d\log M_h}u(k,M_h,z) + \frac{dj_{\nu,sub}}{d\log M_h}\frac{dj_{\nu',sub}}{d\log M_h}u^2(k,M_h,z)\Bigg]\left(\frac{d^2N}{d\log M_h dV}\right)^{-1} dz d\log M_h \tag{11}$$

where $\frac{d^2N}{d\log M_h dV} = \frac{dn}{d\log M_h}$ is the halo-mass function, $u(k, M_h, z)$ is the Fourier transform of the density profile describing the density distribution inside the halo (here we consider the density distribution to be a NFW profile Navarro et al. 1997) and $\frac{dj(\nu,z)}{d\log M_h}$ is the specific emissivity of the central and satellite subhalos at a given frequency and redshift for a given halo mass as defined in Béthermin et al. (2013). Therefore, once we calculate the specific emissivity term for the central and the satellite terms, it is straightforward to calculate the 1-halo power spectrum. Note that for simplicity, we have omitted the M_h and z dependance from $\frac{dj_{\nu,c}}{d\log M_h}$ and $\frac{dj_{\nu,sub}}{d\log M_h}$ terms from all the equations.
For the central galaxies, the differential emissivity is calculated as:

$$\frac{dj_{\nu,c}}{d\log M_h}(M_h,z) = \frac{d^2N}{d\log M_h dV} \times \chi^2(1+z) \times \frac{\mathrm{SFR}_c}{K} \times S^{\rm eff}_\nu(z) \tag{12}$$

where $S^{eff}_\nu(z)$ is the effective SED of the IR galaxies at a given redshift for a given frequency. SFR_c is the star formation rate for the central galaxies with a given halo mass (Eq. 9). K is the Kennicutt constant ($K = \mathrm{SFR}/L_{\rm IR}$) which has a value of $1 \times 10^{-10} M_\odot \mathrm{yr}^{-1} \mathrm{L}_\odot{}^{-1}$ for a Chabrier IMF with $L_{\rm IR}$ being the IR luminosity (8-1000μm).
For the satellite galaxies in the subhalos (Béthermin et al., 2013)

$$\frac{dj_{\nu,sub}}{d\log M_h}(M_h,z) = \frac{d^2N}{d\log M_h dV} \times \chi^2(1+z) \times \int \frac{dN}{d\log m_{\rm sub}}(m_{\rm sub}|M_h)\frac{\mathrm{SFR}_{\rm sub}}{K} \times S^{eff}_\nu(z) \times d\log m_{\rm sub} \tag{13}$$

where $\frac{dN}{d\log m_{\rm sub}}$ is the sub-halo mass function for the satellite galaxies with a sub-halo mass $m_{\rm sub}$. The effective SEDs $S^{eff}_\nu(z)$ for the satellite galaxies are assumed to be the same as the central galaxies. The $\mathrm{SFR}_{\rm sub}$ is calculated using Eqs. 9 and 10 and then smaller of the two values is taken as the SFR value for those galaxies.
In our analysis, we assume a halo mass function from Tinker et al. (2008) and subhalo mass function from Tinker & Wetzel (2010). $S^{eff}_\nu(z)$ are the same ones we used for the linear clustering model of the CIB anisotropies from Maniyar et al. (2018). They have been computed using the method presented in Béthermin et al. (2013) but assuming the new updated SEDs calibrated with the *Herschel* data and presented in Béthermin et al. (2015) and Béthermin et al. (2017). Namely, a stacking analysis is used to measure the evolution of the average mid-infrared to milimeter emission of the massive star forming galaxies up to $z = 4$. Using this technique, it is found that for the main sequence galaxies used in the analysis, the mean intensity of the radiation field which is strongly correlated with the dust temperature rises with redshift. Thus the dust in these new SED templates is warmer at $z > 2$ compared to the previous templates used in Béthermin et al. (2013). We prefer these templates over the other templates (e.g. from Gispert et al. (2000) using FIRAS measurements) as it reproduces all recent measurements of galaxy counts from the mid-IR to the radio wavelength range, including counts per redshift slice.
The Fourier transform of the NFW profile is given as (e.g. van den Bosch et al., 2013)

$$u(k,M_h,z) = \frac{3\delta_{200}}{200c^3}\Bigg(\cos(\mu)[\mathrm{Ci}(\mu+\mu c)-\mathrm{Ci}(\mu)] + \sin(\mu)[\mathrm{Si}(\mu+\mu c)-\mathrm{Si}(\mu)] - \frac{\sin(\mu c)}{\mu+\mu c}\Bigg), \tag{14}$$

where it is to be noted that c is not the speed of light; it is the so called halo concentration parameter defined as $c(M_h, z) \equiv r_{200}(M_h, z)/r_\star(M_h, z)$ with $r_\star(M_h, z)$ being a characteristic radius (see e.g. Navarro et al., 1997) and r_{200} being the radius containing the mass giving 200 times the critical density of the Universe at a redshift (some studies use average density instead of the critical; here we use the critical density), $\mathrm{Ci}(x)$ and $\mathrm{Si}(x)$ are standard cosine and sine integrals respectively, $\mu \equiv kr_\star$ where δ_{200} is a dimensionless amplitude which can be expressed in terms of the halo concentration parameter as

$$\delta_{200} = \frac{200}{3}\frac{c^3}{\ln(1+c) - \frac{c}{1+c}} \tag{15}$$

The 2-halo term for the power spectrum of the CIB takes into account the clustering between galaxies in two different halos of mass M_h and M'_h and is calculated as (Béthermin et al., 2013) (where $k = \ell/\chi$)

$$C^{2h}_{\ell,\nu,\nu'} = \int\int\int \frac{d\chi}{dz}\left(\frac{a}{\chi}\right)^2 \left[\frac{dj_{\nu,c}}{d\log M_h} + \frac{dj_{\nu,sub}}{d\log M_h}u(k,M_h,z)\right] \times \left[\frac{dj_{\nu',c}}{d\log M'_h} + \frac{dj_{\nu',sub}}{d\log M'_h}u(k,M_h,z)\right] \times b(M_h,z)b(M'_h,z)P_{\rm lin}(k,z)d\log M_h\, d\log M'_h\, dz\,, \tag{16}$$

where $b(M_h, z)$ is the halo bias prescription given by Tinker et al. (2010), $P_{\rm lin}(k, z)$ is the linear matter power spectrum which we calculate using `CAMB`[2]. It has to be noted here that

[2] `http://camb.info/`

we use the $u(k, M_h, z)$ term only for the subhalos. This means that in our analysis, the central galaxy is assumed to be at the center of the halo and the satellite galaxies in the subhalos are distributed according to the NFW profile. The clustering term given by $b(M_h, z)b(M'_h, z)P_{\rm lin}(k, z)$ provides cross-power spectrum between two different halos (M_h and M'_h) under the assumption (Cooray & Sheth, 2002) $P(k, M_h, M'_h) = b(M_h, z)b(M'_h, z)P_{\rm lin}(k, z)$. We can simplify Eq. 16 by defining

$$D_\nu(k, z) = \int b(M_h, z)\Big[\frac{d j_{\nu,c}}{d\log M_h} + \frac{d j_{\nu,sub}}{d\log M_h}u(k, M_h, z)\Big]d\log M_h \tag{17}$$

which is the emissivity of the halo weighted by the corresponding bias. Therefore, Eq. 16 becomes (where $k = \ell/\chi$)

$$C^{2h}_{\ell,\nu,\nu'} = \int \frac{d\chi}{dz}\Big(\frac{a}{\chi}\Big)^2 D_\nu(k, z)D'_\nu(k, z)P_{\rm lin}(k, z)dz \tag{18}$$

This way of calculating the 2-halo term significantly reduces the time as it reduces the number of integrals. It is also useful while calculating the CIB-CMB lensing cross-correlation (see Sec. 2.5). Finally we have

$$C^{\rm CIB,clustered}_{\ell,\nu,\nu'} = C^{1h}_{\ell,\nu,\nu'} + C^{2h}_{\ell,\nu,\nu'}\,, \tag{19}$$

and

$$C^{\rm CIB,tot}_{\ell,\nu,\nu'} = C^{1h}_{\ell,\nu,\nu'} + C^{2h}_{\ell,\nu,\nu'} + C^{\rm shot}_{\ell,\nu,\nu'}\,. \tag{20}$$

where $C^{\rm CIB,clustered}_{\ell,\nu,\nu'}$ and $C^{\rm CIB,tot}_{\ell,\nu,\nu'}$ describe the clustered and total CIB anisotropy power spectrum respectively. $C^{\rm shot}_{\ell,\nu,\nu'}$ is the shot-noise component which we can not predict using our halo model formalism here. The shot-noise component is scale independent and thus has a constant flat power spectrum for a given frequency combination. We thus fit for this constant directly at every frequency channel as described in Sec. 3.1.

2.4. $\rho_{\rm SFR}$

Once we have the formalism to calculate the CIB angular power spectrum in the halo modelling context, it is desirable that the halo model is able to fit/reproduce statistical properties of dusty star-forming galaxies, like the infrared (IR) SFRD of the Universe. In the context of our halo model, the SFRD for the central galaxies is calculated as

$$\mathrm{SFRD}_c(z) = \int \frac{d^2N}{d\log M_h dV} \times \mathrm{SFR}(M_h, z) \times d\log M_h \tag{21}$$

and for the satellite galaxies in the subhalos as

$$\mathrm{SFRD}_{\rm sub}(z) = \int \frac{d^2N}{d\log M_h dV}\Big(\int \frac{dN}{d\log m_{\rm sub}} \times \mathrm{SFR}(m_{\rm sub}, z) \times d\log m_{\rm sub}\Big) \times d\log M_h\,, \tag{22}$$

where $\mathrm{SFR}(m_{\rm sub}, z)$ is the satellite galaxy SFR calculated as explained in Sec. 2.2.
Thus, the total SFRD is calculated by adding Eq. 21 and 22 as

$$\mathrm{SFRD}(z) = \mathrm{SFRD}_c(z) + \mathrm{SFRD}_{\rm sub}(z) \tag{23}$$

2.5. CIB-CMB lensing cross-correlation

The large-scale distribution of the matter in the Universe gravitationally deflects the CMB photons propagating freely towards us from the last scattering surface. This phenomenon is called the gravitational lensing which leaves imprints on the temperature and polarisation anisotropies of the CMB. As the CIB is an excellent tracer of the large scale structure of the Universe (Maniyar et al., 2019), its anisotropies are expected to have a strong correlation with the CMB lensing, which has indeed been observed and measured (Planck Collaboration et al., 2014b). Within the context of our halo model, we can calculate this CIB-CMB lensing cross-correlation as (Béthermin et al., 2013) (where $k = \ell/\chi$)

$$C^{\nu\phi}_\ell = \int \frac{d\chi}{dz}\Big(\frac{a}{\chi}\Big) D_\nu(k, z)\Phi(\ell, z)P_{\rm lin}(k, z)dz\,, \tag{24}$$

where $\Phi(\ell, z)$ is given by (Challinor & Lewis, 2005)

$$\Phi(\ell, z) = \frac{3}{\ell^2}\Omega_m\Big(\frac{H_0}{c}\Big)^2\frac{\chi}{a}\Big(\frac{\chi_\star - \chi}{\chi_\star\chi}\Big), \tag{25}$$

In this equation, $\chi_\star$ is comoving distance to the last scattering surface, Ω_m is the matter density parameter, H_0 is the value of the Hubble parameter today, and a is the scale factor of the Universe. The measurement of this cross-correlation is not used in our likelihood to fit the CIB model parameters, but we will see that our best fit model accurately predicts this cross-correlation.

3. Constraints on the model through data

3.1. Observational constraints on the power spectra

We used the CIB angular power spectra as measured by Planck Collaboration et al. (2014c). The measurements were obtained by cleaning the CMB and Galactic dust from the *Planck* frequency maps. They were further corrected for the SZ and spurious CIB contamination induced by the CMB template, as discussed in Planck Collaboration et al. (2014c). We used the measurements at the four highest frequencies (217, 353, 545, and 857 GHz from the HFI instrument). The CIB×CIB power spectra have been corrected for absolute calibration difference between the PR1 and PR2 data release of Planck. Absolute calibration uncertainties for PR2 are equal to 6.1% and 6.4% at 545 and 857 GHz (among which 5% is coming from planets model), respectively (Planck Collaboration et al., 2016a). However, it has been shown that the planet calibration agrees with CMB calibrations within 1.5% for 545 GHz (Planck Collaboration et al., 2016e).
We also used the CIB power spectra measurement from *Herschel*/SPIRE data at 600, 857, and 1200 GHz provided by Viero et al. (2013a). Bertincourt et al. (2016) calculated the cross-calibration factors between the power spectra measured by Viero et al. (2013a) at 600 and 857 GHz and the power spectra measured by Planck Collaboration et al. (2014c) at 545 and 857 GHz and find them to be 1.047 ± 0.0069 and 1.003 ± 0.0080 respectively (for the *Planck* PR2 data release). Absolute calibration uncertainties for these SPIRE data amounts to 9.5%.

Planck and *Herschel* measurements are given with the νI_ν = *constant* photometric convention. As a result, the power spectra computed by the model need to be colour corrected from the CIB SEDs to this convention. These colour corrections are 1.119,

1.097, 1.068, and 0.995 at 217, 353, 545, and 857 GHz, respectively for *Planck* (Planck Collaboration et al., 2014c). They are equal to 0.974, 0.989, and 0.988 for 600, 857, and 1200 GHz channels of *Herschel*/SPIRE, respectively, using the extended relative spectral response function (Lagache et al., 2019). The CIB power spectra are then corrected as

$$C^{\rm model}_{\ell,\nu,\nu'} \text{ x } \text{cc}_\nu \text{ x } \text{cc}_{\nu'} = C^{\rm measured}_{\ell,\nu,\nu'}. \quad (26)$$

The CIB power spectra error bars do not account for the absolute calibration uncertainties. To account for these uncertainties Béthermin et al. (2011) introduce a calibration factor $f^{\nu}_{\rm cal}$ for galaxy number counts. Using a similar approach here, for every frequency channel, we put a Gaussian prior on these calibration factors. As the Herschel power spectra have been cross-calibrated with respect to the Planck power spectra, we fix the calibration factors at the Planck frequencies at 1 and put Gaussian priors on calibration factors $f^{\nu}_{\rm cal}$ for 600 and 857, and 1200 GHz channels from *Herschel*/SPIRE with an initial value of 1.047, 1.003, and 1.000 with 1σ error bars at 0.0069, 0.0080, and 0.0500 respectively (Bertincourt et al., 2016).

Using only *Planck*/HFI data, it is hard to differentiate between the 1-halo and the shot noise term and therefore, Planck Collaboration et al. (2014c) put strong flat priors on the shot noise at all the frequencies. They take values of the shot noise by using the model from Béthermin et al. (2012) with the width of the prior given by their 1σ error bars. However, using *Herschel*/SPIRE data, the CIB power spectra have been measured till very small scales ($\ell_{\rm max} \sim 30360$). At these highest multipoles, the power spectra are dominated by the shot noise and therefore, using these data it is possible to constrain the shot noise together with the 1-halo term better than using the *Planck*/HFI data alone. Thus this paves the way to include shot noise as a parameter for every pair of the power spectra with broad priors i.e. 10 shot noise parameters for HFI as done by Planck Collaboration et al. (2014c) and 6 for SPIRE data. That would be 16 extra parameters. In order to circumvent this problem, we calculate the correlation between the 10 shot noise parameters for HFI and 6 for SPIRE using their values predicted by the model of Béthermin et al. (2012). We then fit for the shot noise parameters for only the auto-power spectra and use the correlation matrix to obtain the shot noise level for every pairs of frequency. Thus, in the end we have only 1 shot noise parameter per frequency i.e. 4 for HFI and 3 for SPIRE. We put broad flat priors on them with sufficient width (10% of the value estimated from Béthermin et al. (2012) model on both sides) not to bias the parameter estimation.

3.2. External observational constraints

In addition to the CIB auto- and cross-power spectra, we used external constraints from the mean CIB intensity values at different frequencies, and the SFRD measurements at different redshifts:

1. As mentioned before, the previously used halo models overpredicted the SFRD of the Universe compared to that measured by external groups using the IR luminosity functions. We would like the halo model to be able to fit the CIB power spectra and also produce the correct SFRD history. Thus, we used the $\rho_{\rm SFR}$ measurements at different redshifts that were obtained by measuring the IR luminosity functions from Gruppioni et al. (2013), Magnelli et al. (2013), Marchetti et al. (2016) as priors while performing the fit. In order to account for the different sets of cosmological parameters used by them, we convert the SFRD values in the observed flux between $8 - 1000\mu m$ per redshift bin per solid angle as done in Maniyar et al. (2018).
   In Appendix A, we show the SFRD history produced by our halo model if this external prior is not considered in the fit. It can be seen that there is, indeed, a significant change in the SFRD history predicted by the model when we do not include any priors at all. Thus including this prior is quite important to get physical results from our model.
2. The mean level of the CIB has been deduced at different frequencies using the galaxy number counts. We use these measurements as constraints on our model. Similar to the case of the power spectra, the mean level of the CIB computed by the model needs to be colour-corrected. The values of the mean level with their corresponding frequencies and the colour corrections we used are given in Table 2 of Maniyar et al. (2018).

3.3. Fitting the data

We performed a Markov chain Monte Carlo (MCMC) analysis on the global CIB parameter space using the Python package 'emcee' (Foreman-Mackey et al., 2013). We have a 14-dimensional parameter space:
- physical model parameters $\{\eta_{\rm max}, M_{\rm max}, \sigma_{M_{h0}}, \tau\}$,
- calibration factors $\{f^{\rm cal}_{600}, f^{\rm cal}_{857}, f^{\rm cal}_{1200}\}$,
- shot noises $\{{\rm SN}^{\rm pl}_{217}, {\rm SN}^{\rm pl}_{353}, {\rm SN}^{\rm pl}_{545}, {\rm SN}^{\rm pl}_{857}, {\rm SN}^{\rm sp}_{600}, {\rm SN}^{\rm sp}_{857}, {\rm SN}^{\rm sp}_{1200}\}$.
The global χ^2 has a contribution from the CIBxCIB, priors on calibration factors, and priors imposed by the external observational constraints mentioned above. We assumed Gaussian uncorrelated error bars for measurement uncertainties which simplifies the covariance matrix ultimately containing only diagonal terms.

3.4. Results

Figures 2 and 3 show the best fit for the halo model to the observational data points for all CIBxCIB auto- and cross-power spectra from *Planck*/HFI and *Herschel*/SPIRE respectively. It is seen that for most of the cases, the 1-halo term is smaller than the shot noise and can potentially be ignored on smaller scales. It is remarkable that we can find a good fit to the data with such a simple model over a wide range of frequencies and multipoles. Based on the best fit parameters and Eq. 24, we calculate the CIBxCMB lensing power spectra. Figure 4 shows these CIBxCMB lensing power spectra. The cross-correlation values and error bars are available for the six Planck HFI channels (100, 143, 217, 353, 545, and 857 GHz) and are provided in Planck Collaboration et al. (2014b). These values range from $\ell = 163$ to $\ell = 1937$ and as discussed in Planck Collaboration et al. (2014b), the non-linear term can be neglected in this range of multipoles. As was done for the CIB, these power spectra have been corrected for absolute calibration difference between the PR1 and PR2 data release of Planck. As can be seen, the best fit model is in very good agreement with the data points.

We present the results from our fit on our model parameters in Table 1. It has to be noted that the shot noise values provided here have to be multiplied with the corresponding colour corrections at each frequency to obtain them in the νI_ν = constant convention. We find a good fit for the model and the posterior of all the parameters with a Gaussian prior (calibration factors) are within a 1σ range of the prior values. We get a χ^2 of 113 for 80 data points for Planck power spectra. Similarly, we get a χ^2 of 247 for Herschel power spectra for 102 data points. When we

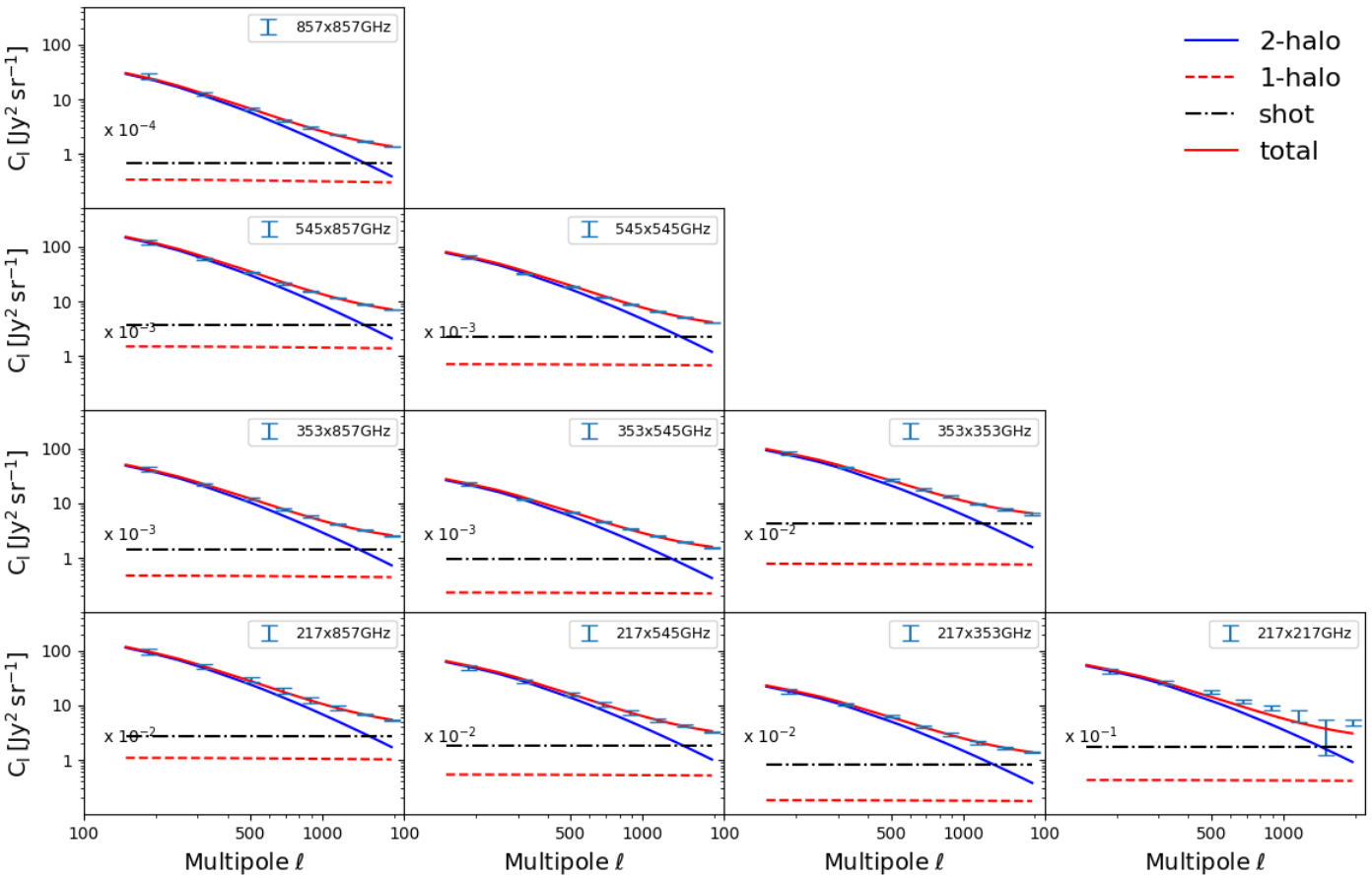

Fig. 2. Measurements of the CIB auto- and cross-power spectra obtained by *Planck*/HFI (Planck Collaboration et al., 2014c) and the best fit CIB halo model with its different components.

only fit for the Planck data without the Herschel power spectrum data but with the external priors, we get a χ^2 of 85 for Planck for 80 data points. Similarly fitting only for the Herschel power spectra with the external priors results in the χ^2 of 221 for 102 data points. Thus when we individually fit for either the Planck or Herschel data, we get a better χ^2 value than when we fit for both of them together.

We also performed this analysis with the updated values of the mean level of the CIB at 350, 350, and 500 μm Herschel/*Spire* bands used as priors in our work (Duivenvoorden et al., 2020). With the updated priors, the χ^2 for Herschel reduces to 222 but the χ^2 for Planck data remains the same.

In all the approaches, the χ^2 value for the Herschel power spectra does not seem to fare as good as the Planck value. Similarly, using a different halo model with a larger number of parameters, Viero et al. (2013a) do not obtain a good χ^2 value ($\chi^2_{\rm reduced} \sim 1.6$). We investigate this problem by checking the compatibility of the Planck and Herschel measurements. The details of the tests we performed are given in Appendix C.
In Fig. C.1, we show the measurements of the CIB power spectra from Planck/HFI (Planck Collaboration et al., 2014c), Herschel/Spire (Viero et al., 2013a), and Lenz et al. (2019) at 857 GHz. We also show the best fit values of the 1-halo, shot noise, and the total power spectrum when the model is fit only to the Planck or Herschel data in black and red color respectively. The Herschel/Spire data points as well as the best fit curves have been scaled to obtain them as they would be measured using the Planck filters at 857 GHz. The procedure for the same has been provided in the Appendix A1 of Lagache et al. (2019). Similar trend is observed for the power spectra at 545 GHz. Wee see that the Herschel and Planck CIB measurement agrees very well at large scale and up to ℓ=2000. But we can also see that the extrapolation of Planck best fit at higher ℓ largely overestimates the Herschel data points. This mostly comes from the shot noises that are not compatible between Planck and Herschel. While the difference of flux cuts (710 mJy for Planck and 300 mJy for Herschel), would give a variation of at most 12% of the shot noise level[3], a factor of ∼1.9 is measured between the two. Note that this discrepancy cannot be reconciled considering the difference in amplitude of the 1-halo term. Such a discrepancy between Herschel and Planck shot noise measurements, as well as with the shot noise values derived from models of galaxy number counts, has already been pointed out by Lagache et al. (2019). Inconsistencies also exist inside a single experiment. For example, we show in Fig. C.2, the comparison of the CIB power spectra measured by Thacker et al. (2013) and Viero et al. (2013a) for the same flux cut of 50 mJy at 857 GHz. The two measurements are clearly different at very high multipoles.

We explore two ways of reconciling the Planck and Herschel measurements using our halo model. In the first approach, we broaden the error bars on the calibration factors for the 600, 857, and 1200 GHz Herschel channels to 0.05 each with their central values at 1.00 instead of using the values obtained for the relative calibration between Planck and Herschel by Bertincourt et al. (2016) as done in our original approach. In this setting, we indeed find a very good fit to the Herschel power spectra, with

[3] The difference in shot noise according to these two flux cuts has been computed using 13 different models we had in hand.

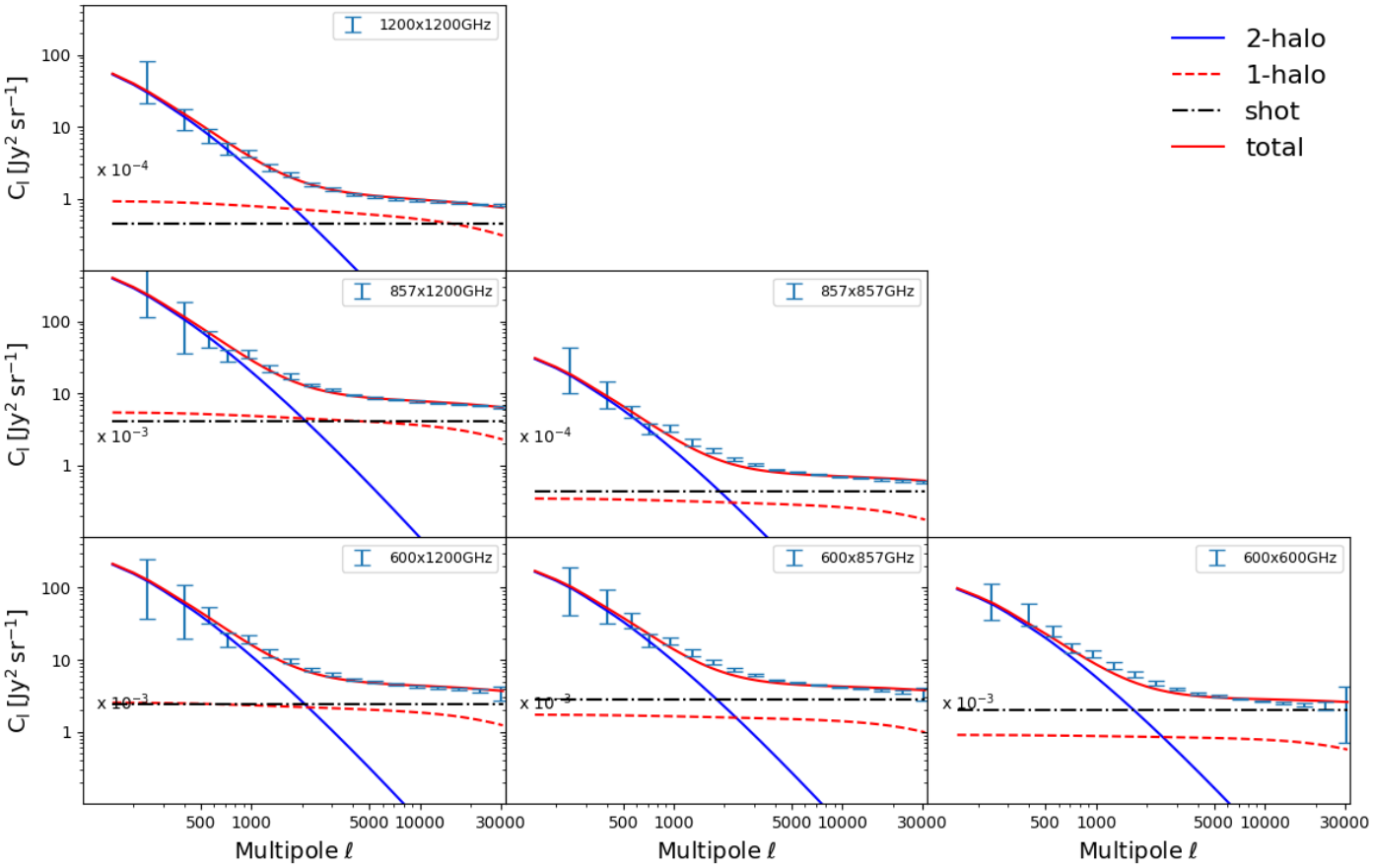

Fig. 3. Measurements of the CIB auto- and cross-power spectra obtained by *Herschel*/SPIRE (Viero et al., 2013a) and the best fit CIB halo model with its different components.

χ^2 of 127 when fit along with Planck data (Tab. C.3), and 137 when only fitting the Herschel data (Tab C.2) compared to χ^2 of 221 before Tab C.4, for 102 data points. However, the best fit value for the calibration factors $f^{\nu}_{\rm cal}$ as shown in Tab. C.3 and C.4 comes out to be too high. As mentioned before, the cross-calibration between Herschel/Spire and Planck/HFI has been measured very precisely at 545 and 857 GHz by Bertincourt et al. (2016) (in fact the 545 GHz Planck channel has been calibrated to better than 1.5%, see Sect.3.1). Thus the best fit values obtained for the $f^{\nu}_{\rm cal}$ parameters are unrealistically high and cannot be accepted. In the second approach, we keep the original priors for the Herschel $f^{\nu}_{\rm cal}$ parameters from Bertincourt et al. (2016) and fit the data for low multipoles only i.e. $\ell < 3000$. Results are provided in Tab. C.5 and Fig. C.3 where we can see that we obtain a good χ^2 (36 for 42 data points) and the shot noise levels for Planck and Herschel come out to be quite similar (see Tab. C.1 and C.5) which is what we expect. This shows that the Herschel data at $\ell > 3000$ are not compatible with the values expected from the $\ell < 3000$ Planck and Herschel data.

With this simple model, $\eta_{\rm max}$ i.e. the maximal efficiency with which the accreted baryonic gas forms into stars is ~40%. It has to be remembered that we do not account for the effects like quenching, AGN and supernovae feedback and their evolution with redshift etc. through explicit parameters. Thus this efficiency parameter $\eta_{\rm max}$ can be seen as the efficiency to convert the accreted baryons into stars after marginalising over these effects. Behroozi et al. (2013) find the baryonic accretion efficiency as defined by us i.e. SFR/BAR to vary between 20-40% across all redshifts which is consistent with our result. Also, Moster et al. (2018) calculate the star formation efficiency as $M_*(z)/M_b(z) = M_*(z)/(M_h(z) \times f_b) = M_*(z)/M_h(z) \times \Omega_m/\Omega_b$ where $M_*(z)$ is the stellar mass in a given halo at a given redshift. They find this value to be 0.17 at redshift $z = 0.1$, and 0.2 at $z = 2.0$. We derived a similar quantity from our model by integrating the mean SFR and BAR over cosmic times for various halo mass seeds at z=10. We find a maximum efficiency of 0.34 at $z = 0.1$ and 0.37 at $z = 2.0$, which is higher than Moster et al. (2018). However, in this approach, we do not take into account the mass loss from stellar evolution. Similar to Zahid et al. (2014), and assuming 45 % mass loss, corresponding to what was found by Leitner & Kravtsov (2011) for an intermediate age galaxy, we find $M_*(z)/M_b(z) = 0.19$ at redshift $z = 0.1$ and 0.21 at $z = 2$. These values are in very good agreement with the previous values of Moster et al. (2018).
Our model provides a non-zero value for τ which means it supports evolution of the width of the lognormal parameterization over time agreeing with the observed suppression of the star formation in massive halos at low redshifts.
We have tried different parameterizations for the η instead of the lognormal. The details of one such parameterization are provided in Appendix B. Due to its simplicity and the ability to provide physical results, we stick with the lognormal parameterization.

Finally, as pointed out in the introduction, one of the shortcomings of the halo model used by Planck Collaboration et al. (2014c) is that it is does not match with the IR SFRD derived

Halo model parameters	$\eta_{\max}$	$\log_{10} M_{\max}$	$\sigma_{M_{h0}}$	τ
$z_c = 1.5$ (fixed)	$0.42^{+0.03}_{-0.02}$	$12.94^{+0.02}_{-0.02}\ M_\odot$	$1.75^{+0.12}_{-0.13}$	$1.17^{+0.09}_{-0.09}$
HFI shot noise	$\mathrm{SN}^{\mathrm{pl}}_{217}$	$\mathrm{SN}^{\mathrm{pl}}_{353}$	$\mathrm{SN}^{\mathrm{pl}}_{545}$	$\mathrm{SN}^{\mathrm{pl}}_{857}$
	$13.88^{+0.71}_{-0.71}$	$353.21^{+9.91}_{-8.66}$	$2003.95^{+37.11}_{-34.16}$	$7036.95^{+190.48}_{-179.71}$
Spire shot noise	$\mathrm{SN}^{\mathrm{sp}}_{600}$	$\mathrm{SN}^{\mathrm{sp}}_{857}$	$\mathrm{SN}^{\mathrm{sp}}_{1200}$	
	$1917.56^{+62.56}_{-54.50}$	$4273.21^{+164.88}_{-148.09}$	$4293.92^{+399.66}_{329.33}$	
HFI/Spire cross-calibration	f^{cal}_{600}	f^{cal}_{857}	f^{cal}_{1200}	
	$1.06^{+0.01}_{-0.01}$	$1.02^{+0.01}_{-0.01}$	$1.04^{+0.03}_{-0.03}$	

Table 1. Marginalised values of all the model parameters given at a 68 % confidence level. The upper row shows the name of the parameter and the row below shows its value. We get a χ^2 value of 113 for 80 data points for Planck, and 247 for 102 data points for Herschel.

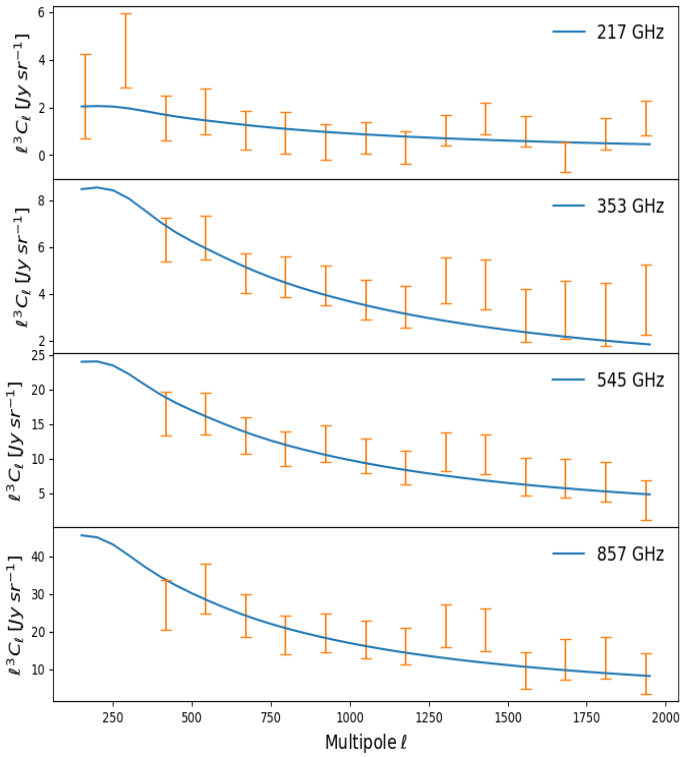

Fig. 4. CIBxCMB lensing cross-power spectra measured by Planck Collaboration et al. (2014b) in orange and our best fit model in blue curves.

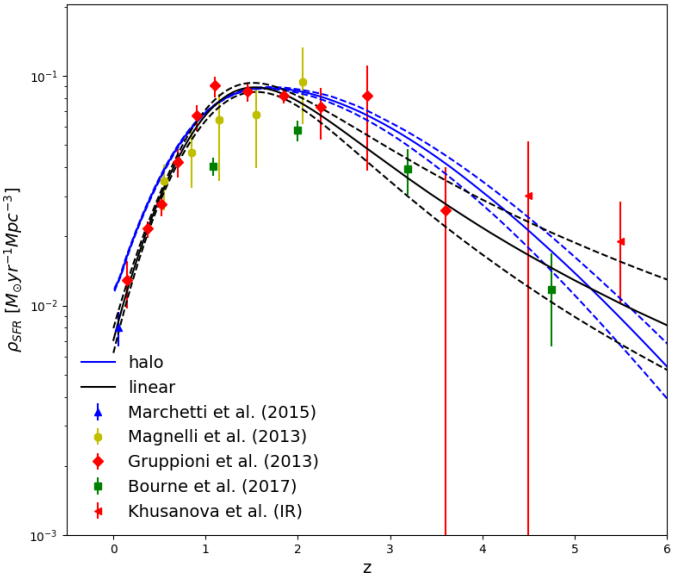

Fig. 5. Measurements of the IR SFRD using galaxies (Madau & Dickinson, 2014). Black (blue) solid line shows the SFRD as constrained by the linear (halo) model with the dotted black (dotted blue) lines showing the 1σ regions around it. We also show the SFRD value determined by Khusanova et al. completely independently using the data from the ALMA ALPINE large program (private communication).

from galaxies. A primary reason for this is that they do not include the independent measurements of the SFRD from galaxy surveys as priors in their likelihood analysis. Consequently, the result from their linear clustering model also is not consistent with the halo model. It is therefore a good consistency check of the model to see if the prediction from the linear model as well as the IR SFRD measurements from galaxies match with the SFRD derived from the best fit of the model. Figure 5 shows the SFRD constrained by our CIB halo model along with the SFRD constrained by the linear model presented in Maniyar et al. (2018). Although at low redshifts the SFRD constrained by the halo model is slightly higher than the measurements from galaxies or the constraints from the linear model, it is overall consistent with the later two. This is again impressive considering the fact that we model the CIB using only four parameters.

4. tSZ halo model

While at lower multipoles ($\ell < 1000$), the tSZ angular power spectrum is sensitive to the amplitude of the matter fluctuations, at higher multipoles ($\ell > 1000$) the power spectrum also depends on the details of the pressure profile of the intra-cluster gas within the halos. Thus, along with the halo mass function, the model also has to account for the pressure profile of the gas. The power spectrum of the tSZ is calculated as (e.g. Bolliet et al., 2018):

$$C^{1h}_{\ell,\nu,\nu'} = f(\nu)f(\nu') \int \frac{dV}{dz} dz \times \int_{m_{\min}}^{m_{\max}} d\log M_h \frac{d^2N}{d\log M_h d\log V} |y_\ell(M_h, z)|^2 \quad (27)$$

where $f(\nu)$ gives the frequency dependance of the tSZ. It is given by

$$f(x) = x\frac{e^x + 1}{e^x - 1} - 4 \ \text{ where } \ x = \frac{h_p \nu_{\mathrm{obs}}}{k_B T_{\mathrm{CMB}}}, \quad (28)$$

where h_p is the Planck's constant, and k_B is the Boltzmann constant. $y_\ell(M_h, z)$ represents the two dimensional Fourier transform of the electron pressure profile P_e for a halo of mass M_h. It is given as (e.g. Komatsu & Seljak, 2001),

$$y_\ell(M_h, z) = \frac{\sigma_T}{m_e c^2} \frac{4\pi r_{500}}{\ell_{500}^2} \int_{x_{\rm min}}^{x_{\rm max}} dx x^2 \frac{\sin(\ell x/\ell_{500})}{\ell x/\ell_{500}} P_e(x)\,. \quad (29)$$

In this equation, c is the speed of the light, σ_T is the Thomson cross-section, m_e is the electron mass, $x \equiv r/r_{500}$ with r being the radial distance from the centre of the halo, r_{500} the radius of the sphere which contains the over-density mass M_{500c} of 500 times the critical density of the universe, and $\ell_{500} \equiv d_A/r_{500}$ with d_A being the angular diameter distance.

As was done for the CIB modelling, we used the NFW profile to represent the density distribution inside the dark-matter halo. Using this distribution, we have

$$P_e(x) = C \times P_0 (c_{500} x)^{-\gamma} [1 + (c_{500} x)^\alpha]^{(\gamma-\beta)/\alpha} \quad (30)$$

where parameters (P_0, c_{500}, γ, α, β) are set to their best-fitting values obtained by Planck Collaboration et al. (2013). They are equal to 6.41, 1.81, 0.31, 1.33, and 4.13, respectively. The coefficient C goes with the mass as

$$C = 1.65 \left(\frac{h}{0.7}\right)^2 \left(\frac{H}{H_0}\right)^{\frac{8}{3}} \left[\frac{(h/0.7)\tilde{M}_{500c}}{3\times10^{14} M_\odot}\right]^{\frac{2}{3}+0.12} \text{eV cm}^{-3}\,, \quad (31)$$

where H is the Hubble's constant at redshift z with H_0 being its local value and h the reduced Hubble's constant ($h = H_0/100$). The mass used here $\tilde{M}_{500_c}$ is not necessarily the true mass but can contain a bias due to observational effects and non-thermal pressure i.e. there can be a difference between the true mass of the cluster and that obtained assuming hydrostatic equilibrium. In order to account for this possible bias, a variable B is often used which relates the true mass M_{500_c} to $\tilde{M}_{500_c}$ as $\tilde{M}_{500_c} = M_{500_c}/B$. In our analysis, we take the mass and redshift range same to that used for the CIB model with $x_{\rm min} = 10^{-6}$ and $x_{\rm max} = 10$ in Eq. 29.

Due to scarcity of massive clusters, the contribution of the 2-halo term to the total tSZ angular power spectrum is quite small compared to the 1-halo term and thus can be neglected (Komatsu & Kitayama, 1999) for $\ell \geq 300$. It is important only for $\ell \leq 300$ but on these scales, the primary CMB anisotropies are clearly dominant. However as we will show in Sec. 5.3, the 2-halo term plays a significant role in the 2-halo term of the CIB×tSZ cross-power spectra and can not be ignored. Thus in our analysis, we do not neglect this component.

It is straightforward to calculate the 2-halo component of the power spectrum as (e.g. Salvati et al., 2018)

$$C^{2h}_{\ell,\nu,\nu'} = f(\nu) f(\nu') \int_{z_{\rm min}}^{z_{\rm max}} \frac{dV}{dz} dz P_{\rm lin}(k = \ell/\chi, z) \left\{ \int_{m_{\rm min}}^{m_{\rm max}} d\log M_h \frac{d^2N}{d\log M_h d\log V} b(M_h, z) y_\ell(M_h, z) \right\}^2 . \quad (32)$$

Thus, the total tSZ power spectrum is the sum of the 1-halo and 2-halo components:

$$C^{\rm tSZ-tot}_{\ell,\nu,\nu'} = C^{1h}_{\ell,\nu,\nu'} + C^{2h}_{\ell,\nu,\nu'}\,. \quad (33)$$

It has to be noted that $f(\nu)$ is negative for $\nu \leq 217$ GHz. This means that the tSZ power spectrum for certain choices of combination of frequencies will be negative. Similar will be the case for the CIB-tSZ correlation described in Sec. 5. To calculate the $f(\nu)$ parameter correctly for a broadband filter, we have to convolve the tSZ frequency dependance with the band pass filter at that particular frequency. The $f(\nu)$ parameter is used to convert the dimensionless y parameter to the CMB temperature units. Although the plots presented here for the tSZ power spectra are made frequency independent (dimensionless) by dividing out the factors of $f(\nu)$, plots for the CIB-tSZ correlation are calculated at the value of the $f(\nu)$ at that particular frequency channel and are convolved with the filters. For 100, 143, 217, 343, 545, and 857 GHz corresponding to the *Planck*/HFI frequencies, f(ν) comes out to be -1.51, -1.04, -0.01, 2.24, 5.60, 11.09 respectively when not convolved with the respective bandpass filters. The effective values become -4.03, -2.79, 0.19, 6.21, 14.46, 26.34 respectively after convolving with the *Planck*/HFI bandpass filters at these respective frequencies as given in Tab.1 of Planck Collaboration et al. (2016d).

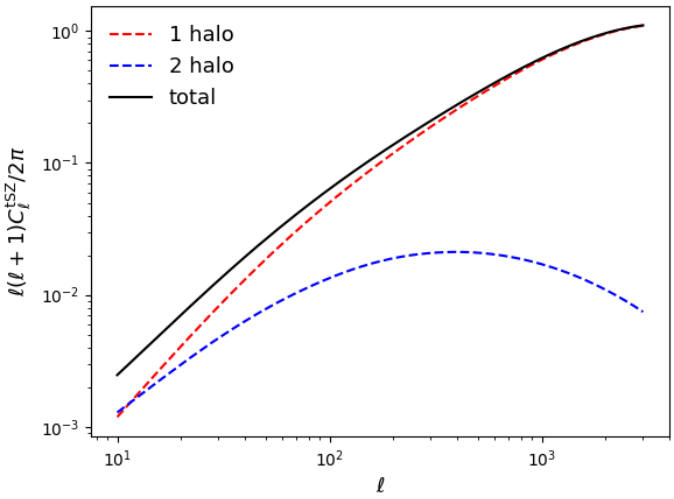

Fig. 6. Predictions for the tSZ power spectrum based on our model for the given values of the parameters. Frequency dependance of the power spectrum through $f(\nu)$ has been divided out and the power spectrum is dimensionless.

As the values of the parameters (P_0, c_{500}, γ, α, β) are not varied, this allows us to tabulate y_ℓ which really speeds up the process. Figure 6 shows the prediction for the tSZ auto-power spectrum with this model and with the given values of the parameters along with B=1.41. The only frequency dependance of the tSZ power spectra comes from the $f(\nu)$ factors and this has been divided out in the plot. As can be seen, around $\ell \sim 1000$ the 2-halo term contributes around 2% to the total power spectrum and the 1-halo term dominates. In their Fig. 1 and 2, Bolliet et al. (2018) show that the tSZ power spectra are very sensitive to the choice of the halo mass function, $c - M_h$ relation (where c is the halo concentration parameter), and cosmological parameters. Thus there are several sources of uncertainties while calculating the tSZ power spectra. At $\ell = 257.5$, using the best fit parameters mentioned before, we get $\ell(\ell+1)\, C_\ell^{\rm tSZ}/2\pi = 0.178$. For this ℓ, Planck Collaboration et al. (2016d) provide the measured y power spectrum ($10^{12} y^2$) value as 0.217 ± 0.049 which is consistent with our predictions (note that the best fit value from their model comes out to be 0.203). We have put here the error bars on the Planck values as the quadrature sum of the statistical and the foreground errors provided by them. At the same time, Bolliet et al. (2018) provide the value of $0.179 \pm +0.034$, with a best fit value of 0.131. This illustrates the range of values the

tSZ power spectra can have based on the different assumptions in the modelling.

5. CIB-tSZ cross-correlation

As pointed out in the introduction, the CIB and tSZ are expected to be correlated to a certain degree. Thus in order to interpret this correlation, we need a cross-correlation model predicting this signal. In the sections before, we presented the halo models to calculate the CIB and the tSZ power spectra and here we use them to calculate the CIB-tSZ correlation in a consistent halo model formalism.

5.1. Halo model formalism

The 1-halo term provides the correlation between the CIB sources and the tSZ within the same halo. On the other hand, the 2-halo term arises due to the correlation between the CIB sources in one halo with the tSZ in other halo. This formulation has a very interesting consequence. Consider an extreme scenario where a very massive halo contributing significantly to the tSZ has no star formation happening within it and hence has no CIB sources. In this case, the 1-halo term would be zero but there would still be a contribution from the 2-halo term provided that there is some overlap in the redshift distribution of the CIB sources and the tSZ halos. Thus the 2-halo term which dominates on the large angular scales, does not depend significantly on the astrophysical processes governing the star formation in massive halos contributing to the tSZ.

The corresponding 1-halo and 2-halo terms are given as (for $k = \ell/\chi$)

$$C^{1h}_{\ell,\nu,\nu'} = \int dz \frac{dV}{dz} \int d\log M_h \frac{d^2N}{d\log M_h d\log V}\, y_\ell \times \Big[\{\frac{dj'_{\nu_1,c}}{d\log M_h} + \frac{dj'_{\nu_1,\rm sub}}{d\log M_h} u(k,M_h,z)\} f(\nu_2) + \{\frac{dj'_{\nu_2,c}}{d\log M_h} + \frac{dj'_{\nu_2,\rm sub}}{d\log M_h} u(k,M_h,z)\} f(\nu_1)\Big], \quad (34)$$

and

$$C^{2h}_{\ell,\nu,\nu'} = \int dz \frac{dV}{dz} P_{\rm lin}(k,z) \times \int d\log M_h \frac{d^2N}{d\log M_h d\log V}\, y_\ell\, b(M_h,z) \times \int d\log M'_h \frac{d^2N}{d\log M'_h d\log V}\, b(M'_h,z) \times \Big[\{\frac{dj'_{\nu_1,c}}{d\log M'_h} + \frac{dj'_{\nu_1,\rm sub}}{d\log M'_h} u(k,M'_h,z)\} f(\nu_2) + \{\frac{dj'_{\nu_2,c}}{d\log M'_h} + \frac{dj'_{\nu_2,\rm sub}}{d\log M'_h} u(k,M'_h,z)\} f(\nu_1)\Big], \quad (35)$$

where

$$\frac{dj'_{\nu,c(\rm sub)}}{d\log M_h}(M_h,z) = \frac{dj_{\nu,c(\rm sub)}}{d\log M_h}(M_h,z) \frac{a}{\chi^2} \Big(\frac{d^2N}{d\log M_h dV}\Big)^{-1}. \quad (36)$$

Note that M_h and M'_h terms while calculating the 2-halo term represent mass of the two different halos between which the correlation is being computed. As the tSZ spectral variation is not dependent on the redshift or halo mass in the non-relativistic limit, the cross spectra are simpler than would be otherwise.
The total CIBxtSZ power is then

$$C^{\rm CIBxtSZ-tot}_{\ell,\nu,\nu'} = C^{1h}_{\ell,\nu,\nu'} + C^{2h}_{\ell,\nu,\nu'}. \quad (37)$$

Thus, once we have the CIB and the tSZ model parameters, it is straightforward to calculate the CIB-tSZ power spectra and there is no need of extra parameter. This is one of the advantages of the halo model approach over the previous studies (e.g. Dunkley et al., 2013, George et al., 2015) where a template based approach for the CIB-tSZ correlation was used by introducing a parameter ξ to act as a correlation coefficient. This template based approach is also limited by the fact that ξ might be angular and scale dependent and hence fitting for a single parameter ξ might not produce a true picture of the CIB-tSZ correlation. This has indeed been shown to be the case by Addison et al. (2012) where they found non-negligible variation in ξ with the angular scales as well as the considered frequencies.

5.2. Halo mass definition

As we have seen, our models for CIB and tSZ (and thus CIB×tSZ) rely on the halo mass M_h. In general for the tSZ effect, the pressure profile from Eq. 30 is given in terms of M_{500} which is defined as the mass contained within a radius where the mean overdensity is 500 times the background critical density. On the contrary, the CIB studies are generally carried out with M_{200} as the definition of the halo mass. Thus, we have to be consistent with the definition of the halo mass while considering the CIB and tSZ together. One of the ways of doing this is calculating the CIB terms with M_{200}, then converting the M_{200} to corresponding M_{500} for the given redshift range and cosmology using the procedure given in Komatsu & Seljak (2001), and then using this M_{500} to calculate the corresponding tSZ terms. While presenting the CIB×tSZ results here though we have worked with a single definition of M_{500} for the halo masses both for the CIB and tSZ terms. We checked the effect of using M_{500} instead of M_{200} on the CIB model parameters and we found that the values of the CIB parameters slightly change. The most notable change was observed in the value of $\eta_{\rm max}$ which was found to be higher when we use M_{500} instead of M_{200}. This can be explained because with this definition of the mass, the CIB contribution is calculated very close to the center of the cluster not counting the star formation happening far away. Thus the model tries to increase the efficiency of conversion of the accreted baryons into stars to produce the same level of CIB as observed. Note that the CIB model parameters given in Tab. 1 have been calculated using the normally used M_{200} definition for the halo masses.

5.3. Predictions for the CIB×tSZ power spectra

Figure 7 shows the predictions for the CIB, tSZ, and CIBxtSZ power spectra correlating the *Planck* 143 GHz frequency with other frequencies based on the models of the CIB, tSZ, and CIBxtSZ given above. It has to be noted again that the results here have been derived using the M_{500} definition for the halo masses and for the tSZ, the $f(\nu)$ factor is convolved with the *Planck*/HFI frequencies giving the values of -4.03, -2.79, 0.19, 6.21, 14.46, 26.34 for 100, 143, 217, 343, 545, and 857 GHz respectively as mentioned in Sec. 4. Thus $f(\nu)$ is negative for $\nu < 217$ GHz and the tSZ power spectra are negative for certain choices of the frequency pairs. In the figure, the tSZ power spectra are negative for a combination of 143 GHz with all the frequencies above 143 GHz i.e. 217, 353, 545, and 857 GHz (we

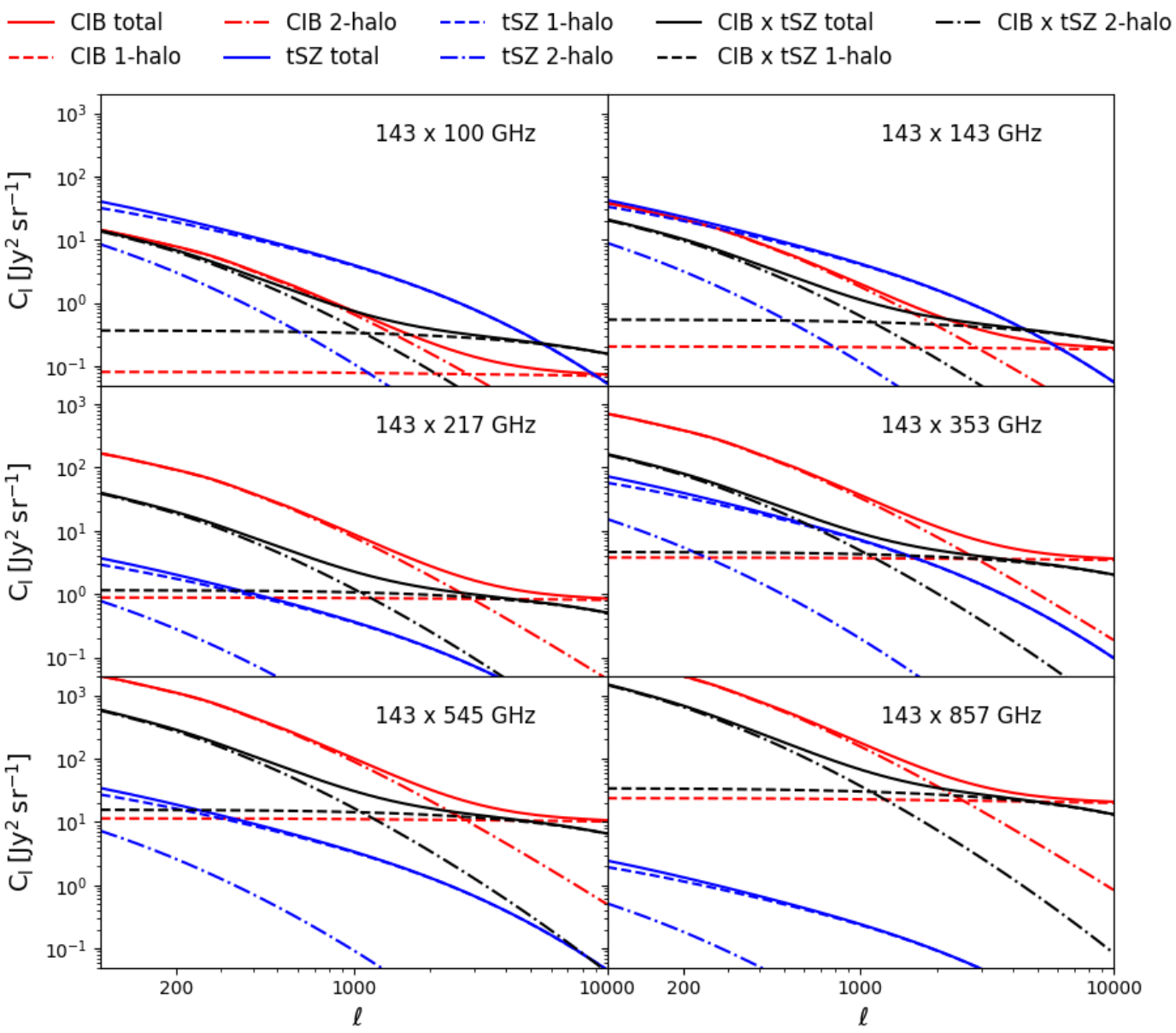

Fig. 7. Predictions for the different components of the CIB, tSZ, and CIBxtSZ power spectra correlating the *Planck* 143 GHz frequency with other frequencies based on the models given above.

show their absolute values). Similarly, CIBxtSZ power spectra shown here are negative in all the cases from 100 to 857 GHz.
A special case to consider while using Eqs. 34 and 35 is that of the two widely separated frequency channels. It can be seen from Fig. 7 that the relative power of the CIB-tSZ to the CIB increases with the frequency separation for frequencies $\nu \geq 217$ GHz. Generally in such a case, due to different frequency dependance of the CIB and tSZ, one of the terms in the square parentheses is much smaller compared to the other one and can be neglected. In this case, the cross-correlation is driven by the dominating term. The CIB at higher frequencies traces the halos at lower redshifts and this increases the overlap with the tSZ clusters. This results in the increase in the CIB-tSZ power compared to the CIB power spectra as the frequency separation increases. Such a scenario can provide a good opportunity to constrain the CIB-tSZ cross-power spectra. The tSZ term dominates at lower frequency channels and drives the cross-correlation. The tSZ has a null point at $\nu \approx 217$ GHz. This can be seen from the figure as well where the tSZ power spectra in 143x217 GHz is much smaller than for 143x143 and 143x353 GHz.
Our predictions are not exactly similar to that obtained by Addison et al. (2012). The observational constraints for the tSZ and especially the CIB have improved dramatically since their results came out. This has manifested in an improved understanding and modelling of both the tSZ and the CIB which we take the advantage of and hence the difference in the predictions.

5.4. Redshift contributions to the power spectra

Figure 8 shows the contributions to the CIB-tSZ power spectra coming from different redshift bins. The power spectra are shown for 100-100 GHz and 100-857 GHz channel pairs with different colours showing different redshift bins with dashed and dot-dashed line showing the 1-halo and 2-halo contributions respectively, and solid lines giving the total power spectra.
The clusters hosting the hot gas with energetic electrons giving

rise to the tSZ effect reside at relatively low redshifts ($\sim z < 1$). Thus, we should expect the contribution of the 1-halo term of the power spectrum to the total power spectrum to relatively decrease compared to the 2-halo term as we go on higher redshifts. This is indeed what we observe in Fig. 8 where as you go higher in the redshift bins, the multipole where the 1-halo and 2-halo term contribute equally moves slightly to higher values i.e. the range over which the 2-halo term dominates over the 1-halo term, increases with redshift. This of course depends upon the width of the redshift bins considered as well as the pair of the frequency channels considered but the overall trend is the same. One important thing to notice from Fig. 8 is that although majority of the tSZ clusters are expected to reside at lower redshifts, the CIB-tSZ contribution coming from the lowest redshift bin ($0 < z < 0.5$) is smaller than or equal to from other redshift bins. In fact, for 100-100 GHz channel pair, our model predicts that the CIB-tSZ contribution coming from $0 < z < 0.5$ is of the same order from the $z > 3$ bin where we do not expect to find a lot of tSZ clusters. While for 100-857 GHz channel pair, the contribution from the $0 < z < 0.5$ redshift bin is higher than the $z > 3$ bin. The CIB at lower frequencies traces the galaxies on higher redshift to certain extent and vice versa. Thus, in the 100-100 GHz case, the CIB contribution is mainly coming from the galaxies at relatively higher redshift (e.g. see Fig. 4 of Maniyar et al., 2018) and thus the 2-halo term caused by the overlap in the redshift distribution of the CIB sources and the tSZ halos gives slightly higher power in the $z > 3$ redshift bin relative to the $0 < z < 0.5$ bin in 100-100 GHz case. Exactly opposite is the case for the 100-857 GHz pair where CIB is mainly sourced by the galaxies at lower redshifts thereby increasing the power in the lowest redshift bin.

Majority of the contribution to the CIB-tSZ power spectra seems to be coming from the intermediate redshift bins i.e. $0.5 < z < 1.5$ and $1.5 < z < 3.0$. Going back to Fig. 4 of Maniyar et al. (2018) again, this is expected because most of the CIB power is coming from the dusty star forming galaxies between $0.5 < z < 4$. Thus the CIB part driving the CIB-tSZ correlation has most of its contribution coming from these redshifts. Again, we can see that going from 100-100 GHz pair to 100-857 GHz pair, the contribution of the $0.5 < z < 1.5$ slightly increases in comparison to $1.5 < z < 3$ bin as even lower redshifts are probed by the CIB at 857 GHz than at 100 GHz.

5.5. Angular scale dependance of the CIB×tSZ power spectra

Measuring the kSZ power spectrum from the CMB power spectrum is one of the challenging goals of the modern day CMB cosmology data analysis. It is important to measure the kSZ power spectrum because it can help us to better understand the reionisation history of the Universe. The kSZ power spectra show up on very small angular scales ($\ell > 2000$) in the CMB power spectra. At these scales the CIB, tSZ, and their correlation act as foregrounds to correctly measure the kSZ. Figures 5 and 6 from George et al. (2015) show that the kSZ is degenerate with the tSZ and CIB×tSZ correlation. Thus a consistent modelling of these foregrounds is highly desirable.

The kSZ has been constrained by Dunkley et al. (2013) and George et al. (2015) using the CMB power spectrum measurements from the Atacama Cosmology Telescope (ACT) and the South Pole Telescope (SPT), respectively, while Planck Collaboration et al. (2016c) reported a measurement of the CIB×tSZ correlation using the Planck data. George et al. (2015) calculate the CIB×tSZ power spectra at every step of their analysis using the CIB and tSZ power spectra obtained using templates at that step, whereas Dunkley et al. (2013) and Planck Collaboration et al. (2016c) use the CIB×tSZ template provided by Addison et al. (2012). All of them fit for a single scale independent amplitude parameter for the CIB×tSZ correlation across all the frequency channels. Addison et al. (2012) use the CIB model from Xia et al. (2012) to calculate the CIB×tSZ cross-correlation. One of the shortcomings of this model is that it assumes the spectral properties of the CIB i.e. SEDs, luminosity to be independent of the host halo mass. Our understanding of the CIB and its properties has improved significantly over the last few years and we know that the spectral properties of the CIB are highly dependent on the host halo mass. Thus we compare the CIB×tSZ correlation calculated with our newly developed CIB halo model with that developed by Addison et al. (2012) using the CIB model from Xia et al. (2012).

Figure 9 shows the ratio of the CIB×tSZ template from Addison et al. (2012) used in the Planck Collaboration et al. (2019) likelihood analysis and the corresponding power spectra calculated within our halo model framework at 217×217 GHz in red color. It has to be noted here that both power spectra are normalised such that they have equal value at $\ell = 3000$. As we can see, the ratio of the CIB×tSZ template used in the Planck Collaboration et al. (2019) with our model is quite different at all scales (e.g. 1.1 at $\ell \sim 2000$ and 0.9 at $\ell \sim 3700$). Thus, the results on the kSZ power spectra derived using such templates might turn out to be quite different than if the halo model developed in this paper is used. In Fig. 9, we also plot the ratio of the CIB×tSZ power spectra for different pairs of Planck frequency channels with that at 217×217 GHz, again normalised such that they have the same value at $\ell = 3000$. We can see that although at very high multipoles the ratio does not vary a lot because the CIB at these nearby frequency channels is highly correlated, it does show variation by up to 10% for $\ell < 2000$. Addison et al. (2012) also show that for widely separated frequency channels, the CIB×tSZ correlation is different at different multipoles. Thus, fitting for a single amplitude parameter independent of the multipoles for the CIB×tSZ power spectra across all frequency channels is a crude approximation. The best fit templates used in the previous analysis should be replaced by such physically motivated halo models.

6. Conclusions

One of the main motivations of this work is to design a consistent framework to calculate the CIB, tSZ and CIB×tSZ power spectra in a halo model setting. For this purpose, we developed a simple and physically motivated halo model of the CIB with only four parameters describing the relationship between the mass of the dark matter halos and their efficiency to convert the accreted baryons into stars using a lognormal parameterization. Due to the previous evidence of massive halos not contributing significantly at lower redshift to the total star formation budget but being efficient at high redshift, we allow the width of the lognormal to evolve with redshift. Using this model, we obtain a good fit simultaneously to both the *Planck* and *Herschel* CIB power spectra We find that the mass of the dark-matter halos for maximal efficiency is $\log_{10} M_{\rm max} = 12.94^{+0.02}_{-0.02}\, M_\odot$, while the maximum efficiency at this mass is $\eta = 0.42^{+0.03}_{-0.02}$. The mass of maximal efficiency found here is slightly on the high side of the range $\log_{10} M = 12.1^{+0.50}_{-0.50}$ $M_\odot$ to $12.6^{+0.10}_{-0.10}$ $M_\odot$ found by Viero et al. (2013a) and Planck Collaboration et al. (2014c) but in very good agreement with Chen et al. (2016) for faint SMGs of $\log_{10} M = 12.7^{+0.1}_{-0.2}$ and $\log_{10} M = 12.77^{+0.128}_{-0.125}$ using the linear clustering model for the CIB anisotropies (Maniyar et al., 2018).

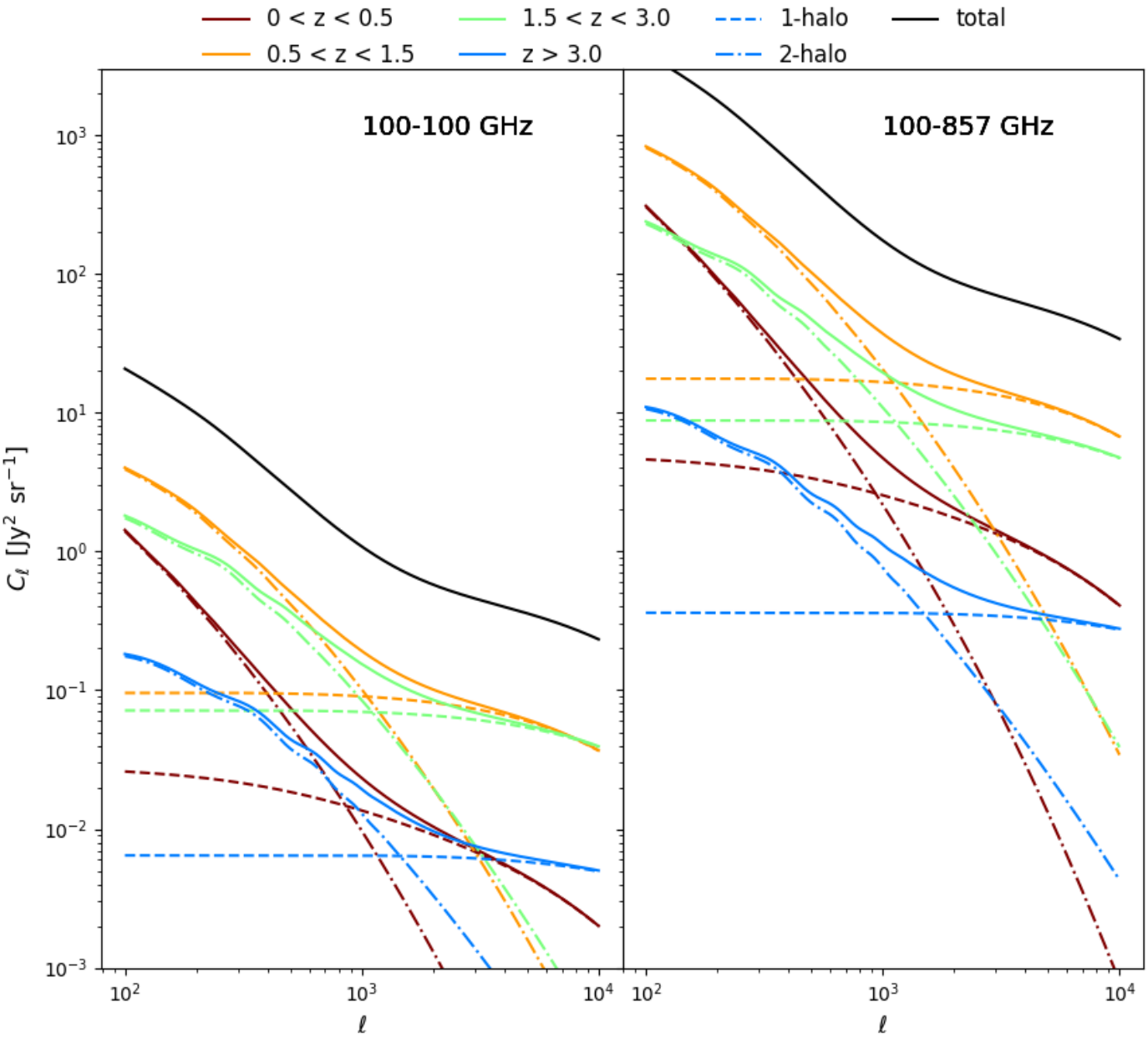

Fig. 8. Redshift contribution to the power spectra of the CIB-tSZ correlation at for 100-100 GHz channel pair (right panel) and 100-857 GHz channel pair (right panel). All the values shown here are absolute values.

This is quite motivating considering the simple nature of our model. The model is also able to fit the SFRD measured using the galaxies and is consistent with the SFRD history obtained using the linear clustering model from Maniyar et al. (2018). This is again a significant result considering that the previous models could not reproduce the SFRD history consistently to their linear counterparts or could not match the observed SFRDs from the galaxies (Planck Collaboration et al., 2014c) mainly because they do not use these independent SFRD measurements as priors in their likelihood analysis. We also calculate the CIB-CMB lensing cross-correlation using the best fit value of the CIB parameters and find that it agrees well with the measurements (Fig. 4). While we get a decent χ^2 of 113 for 80 Planck data points, the χ^2 for Herschel power spectra comes out to be 247 for 102 data point which is not good. We investigate this discrepancy using different methods and find that the CIB power spectrum measurements are not fully compatible with each other for ℓ >3000.

For the tSZ, we follow the approach of Bolliet et al. (2018) and develop a halo model to calculate the 1-halo and 2-halo power spectra. As we keep the parameters for the pressure profile of the gas constant, the power spectra calculations are sped up by tabulating the values of y_ℓ. The only parameter for the tSZ power spectra is the mass bias B which takes into account the difference between e.g. the true halo mass and the mass derived assuming the hydrostatic equilibrium. Although we find that the contribution of the 2-halo term is not significant $\sim$ 2% at $\ell \sim 1000$ to the total power spectra, we still consider it in our calculations for a complete analysis and because the 2-halo term has a significant contribution to the 2-halo term of the CIB×tSZ which is significant and can not be ignored.

Following our two halo models for the CIB and tSZ, we compute the cross-correlation between the CIB and tSZ within a halo model framework. Apart from being consistent with the CIB

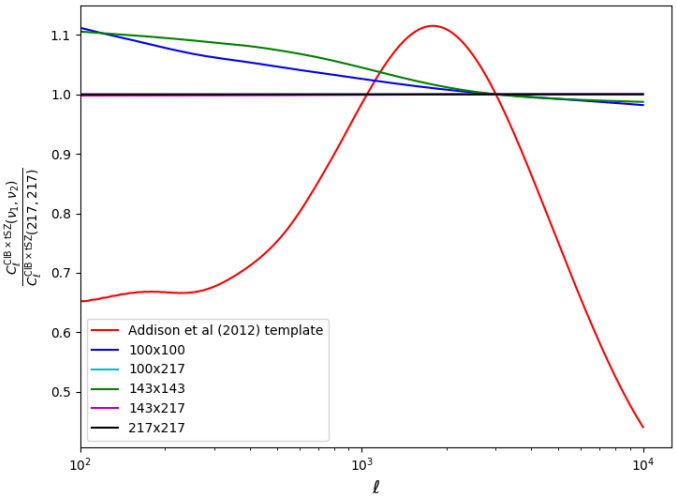

Fig. 9. Ratio of the CIB×tSZ correlation at different frequencies and at 217×217 GHz. The red curve shows the ratio with the CIB×tSZ template from Addison et al. (2012) used in the Planck Collaboration et al. (2019) likelihood analysis. All the power spectra are normalised such that they have the same value at $\ell = 3000$.

and the tSZ halo models, another advantage of this approach is that we do not require an extra parameter to calculate the correlation. Once we know the CIB and tSZ model parameters, it is straightforward to calculate the CIB-tSZ correlation. This is quite advantageous over other studies where the template approach for the power spectra is used and a fit for the global amplitude is performed. Based on our model and the best fit of the CIB and tSZ parameters, we find that the relative power of the CIB-tSZ correlation with respect to the CIB and tSZ increases with the frequency separation of the maps. We also see that the two halo term for the CIB-tSZ correlation is not negligible with respect to the 1-halo term and should be considered in the total power spectrum calculation. This 2-halo term arises due to the correlation between the tSZ being sourced from a halo and the CIB galaxies residing in the other halo. Also, we see that majority of the contribution to the CIB-tSZ power spectra comes from $0.5 < z < 4$ as the CIB part contributing to the CIB-tSZ correlation has most of its power coming from these redshifts.

CIB and tSZ act as foregrounds in CMB anisotropy measurements. Especially on small scales the CIB, tSZ, and CIB×tSZ correlation act as a hinderance to measure the kinetic SZ (kSZ) signal which is the SZ effect caused by the peculiar velocities of the galaxy clusters after reionisation as well as by the ionised bubbles during the reionisation. Thus, in order to measure the kSZ from the CMB power spectrum, it is important to correctly model and remove the above mentioned foregrounds. Previous analyses to measure the kSZ power spectra have used a template based approach to model the foregrounds and fit for a single amplitude parameter across all the frequency channels independent of the multipole range considered. We showed that this approach is not sufficient to capture the scale dependence of the CIB×tSZ power spectra, which is moreover model dependent. Similar argument is also applicable to modelling the other foregrounds i.e. the CIB and tSZ as well. The kSZ constraints obtained using the template approach have thus to be revised, replacing the templates by power spectra computed by the physically developed halo models. Considering the effectiveness of our halo model, it can potentially be used for this purpose.

Acknowledgements. We acknowledge financial support from the "Programme National de Cosmologie and Galaxies" (PNCG) funded by CNRS/INSU-IN2P3-INP, CEA and CNES, France and support from the OCEVU Labex (ANR-11-LABX-0060) and the A*MIDEX project (ANR-11-IDEX-0001-02) funded by the "Investissements d'Avenir" French government program managed by the ANR. GL has received funding from the European Research Council (ERC) under the European Union's Horizon 2020 research and innovation programme (grant agreement No 788212) and funding from the Excellence Initiative of Aix-Marseille University-A*Midex, a French "Investissements d'Avenir" programme". AM warmly thanks Marco Tucci for useful discussions and inputs on the halo modelling of the CIB power spectra.

References

Addison, G. E., Dunkley, J., & Spergel, D. N. 2012, MNRAS, 427, 1741
Amblard, A. & Cooray, A. 2007, ApJ, 670, 903
Amblard, A., Cooray, A., Serra, P., et al. 2011, Nature, 470, 510
Behroozi, P. S., Wechsler, R. H., & Conroy, C. 2013, The Astrophysical Journal, 770, 57
Bertincourt, B., Lagache, G., Martin, P. G., et al. 2016, A&A, 588, A107
Béthermin, M., Daddi, E., Magdis, G., et al. 2015, A&A, 573, A113
Béthermin, M., Daddi, E., Magdis, G., et al. 2012, ApJ, 757, L23
Béthermin, M., Dole, H., Lagache, G., Le Borgne, D., & Penin, A. 2011, A&A, 529, A4
Béthermin, M., Wang, L., Doré, O., et al. 2013, A&A, 557, A66
Béthermin, M., Wu, H.-Y., Lagache, G., et al. 2017, A&A, 607, A89
Bolliet, B., Comis, B., Komatsu, E., & Macías-Pérez, J. F. 2018, MNRAS, 477, 4957
Cantalupo, S., Lilly, S. J., & Haehnelt, M. G. 2012, MNRAS, 425, 1992
Chabrier, G. 2003, PASP, 115, 763
Challinor, A. & Lewis, A. 2005, Phys. Rev. D, 71, 103010
Chen, C.-C., Smail, I., Swinbank, A. M., et al. 2016, ApJ, 831, 91
Cooray, A. & Sheth, R. 2002, Phys. Rep., 372, 1
Cousin, M., Guillard, P., & Lehnert, M. D. 2019, arXiv e-prints, arXiv:1901.01906
Cousin, M., Lagache, G., Bethermin, M., & Guiderdoni, B. 2015, A&A, 575, A33
Daddi, E., Bournaud, F., Walter, F., et al. 2010, ApJ, 713, 686
Dessauges-Zavadsky, M., Zamojski, M., Schaerer, D., et al. 2015, A&A, 577, A50
Duivenvoorden, S., Oliver, S., Béthermin, M., et al. 2020, MNRAS, 491, 1355
Dunkley, J., Calabrese, E., Sievers, J., et al. 2013, Journal of Cosmology and Astro-Particle Physics, 2013, 025
Fakhouri, O., Ma, C.-P., & Boylan-Kolchin, M. 2010, MNRAS, 406, 2267
Foreman-Mackey, D., Hogg, D. W., Lang, D., & Goodman, J. 2013, PASP, 125, 306
George, E. M., Reichardt, C. L., Aird, K. A., et al. 2015, ApJ, 799, 177
Gispert, R., Lagache, G., & Puget, J. L. 2000, A&A, 360, 1
Gruppioni, C., Pozzi, F., Rodighiero, G., et al. 2013, MNRAS, 436, 2875
Hanson, D., Hoover, S., Crites, A., et al. 2013, Physical Review Letters, 111, 141301
Kereš, D., Katz, N., Weinberg, D. H., & Davé, R. 2005, MNRAS, 363, 2
Knox, L., Cooray, A., Eisenstein, D., & Haiman, Z. 2001, ApJ, 550, 7
Komatsu, E. & Kitayama, T. 1999, ApJ, 526, L1
Komatsu, E. & Seljak, U. 2001, MNRAS, 327, 1353
Lagache, G., Bavouzet, N., Fernandez-Conde, N., et al. 2007, ApJ, 665, L89
Lagache, G., Bethermin, M., Montier, L., Serra, P., & Tucci, M. 2019, arXiv e-prints, arXiv:1911.09466
Lagache, G. & Puget, J. L. 2000, A&A, 355, 17
Leitner, S. N. & Kravtsov, A. V. 2011, ApJ, 734, 48
Lenz, D., Doré, O., & Lagache, G. 2019, ApJ, 883, 75
Limber, D. N. 1954, ApJ, 119, 655
Madau, P. & Dickinson, M. 2014, ARA&A, 52, 415
Magnelli, B., Popesso, P., Berta, S., et al. 2013, A&A, 553, A132
Maniyar, A., Lagache, G., Béthermin, M., & Ilić, S. 2019, A&A, 621, A32
Maniyar, A. S., Béthermin, M., & Lagache, G. 2018, A&A, 614, A39
Marchetti, L., Vaccari, M., Franceschini, A., et al. 2016, MNRAS, 456, 1999
Matsuhara, H., Kawara, K., Sato, Y., et al. 2000, A&A, 361, 407
Miller, T. B., Chapman, S. C., Aravena, M., et al. 2018, Nature, 556, 469
Moster, B. P., Naab, T., & White, S. D. M. 2013, MNRAS, 428, 3121
Moster, B. P., Naab, T., & White, S. D. M. 2018, Monthly Notices of the Royal Astronomical Society, 477, 1822–1852
Navarro, J. F., Frenk, C. S., & White, S. D. M. 1997, ApJ, 490, 493
Planck Collaboration, Adam, R., Ade, P. A. R., et al. 2016a, A&A, 594, A8
Planck Collaboration, Ade, P. A. R., Aghanim, N., et al. 2014a, A&A, 571, A21
Planck Collaboration, Ade, P. A. R., Aghanim, N., et al. 2014b, A&A, 571, A18
Planck Collaboration, Ade, P. A. R., Aghanim, N., et al. 2014c, A&A, 571, A30
Planck Collaboration, Ade, P. A. R., Aghanim, N., et al. 2013, A&A, 550, A131

Planck Collaboration, Ade, P. A. R., Aghanim, N., et al. 2011, A&A, 536, A18
Planck Collaboration, Ade, P. A. R., Aghanim, N., et al. 2016b, A&A, 594, A13
Planck Collaboration, Ade, P. A. R., Aghanim, N., et al. 2016c, A&A, 594, A23
Planck Collaboration, Aghanim, N., Akrami, Y., et al. 2019, arXiv e-prints, arXiv:1907.12875
Planck Collaboration, Aghanim, N., Arnaud, M., et al. 2016d, A&A, 594, A22
Planck Collaboration, Aghanim, N., Ashdown, M., et al. 2016e, A&A, 596, A107
Popesso, P., Biviano, A., Finoguenov, A., et al. 2015, A&A, 579, A132
Puget, J.-L., Abergel, A., Bernard, J.-P., et al. 1996, A&A, 308, L5
Reichardt, C. L., Shaw, L., Zahn, O., et al. 2012, ApJ, 755, 70
Saintonge, A., Lutz, D., Genzel, R., et al. 2013, ApJ, 778, 2
Salvati, L., Douspis, M., & Aghanim, N. 2018, A&A, 614, A13
Shang, C., Haiman, Z., Knox, L., & Oh, S. P. 2012, MNRAS, 421, 2832
Silk, J. 2003, MNRAS, 343, 249
Somerville, R. S., Hopkins, P. F., Cox, T. J., Robertson, B. E., & Hernquist, L. 2008, MNRAS, 391, 481
Thacker, C., Cooray, A., Smidt, J., et al. 2013, ApJ, 768, 58
Tinker, J., Kravtsov, A. V., Klypin, A., et al. 2008, ApJ, 688, 709
Tinker, J. L., Robertson, B. E., Kravtsov, A. V., et al. 2010, ApJ, 724, 878
Tinker, J. L. & Wetzel, A. R. 2010, ApJ, 719, 88
van den Bosch, F. C., More, S., Cacciato, M., Mo, H., & Yang, X. 2013, MNRAS, 430, 725
Viero, M. P., Ade, P. A. R., Bock, J. J., et al. 2009, ApJ, 707, 1766
Viero, M. P., Wang, L., Zemcov, M., et al. 2013a, ApJ, 772, 77
Viero, M. P., Wang, L., Zemcov, M., et al. 2013b, ApJ, 772, 77
Wang, T., Elbaz, D., Daddi, E., et al. 2018, ApJ, 867, L29
Xia, J.-Q., Negrello, M., Lapi, A., et al. 2012, MNRAS, 422, 1324
Zahid, H. J., Dima, G. I., Kudritzki, R.-P., et al. 2014, The Astrophysical Journal, 791, 130

Appendix A: The SFRD prior importance

Along with providing a good fit to the CIB power spectra, the halo model should be able to reproduce the SFRD history measured by extrapolating the galaxy luminosity functions. For this reason, we used the SFRD measurements from galaxies at different redshifts as priors while fitting for the halo model parameters. The best fit parameters then result in the SFRD history as shown in Fig. 5 which is consistent with the external measurements.

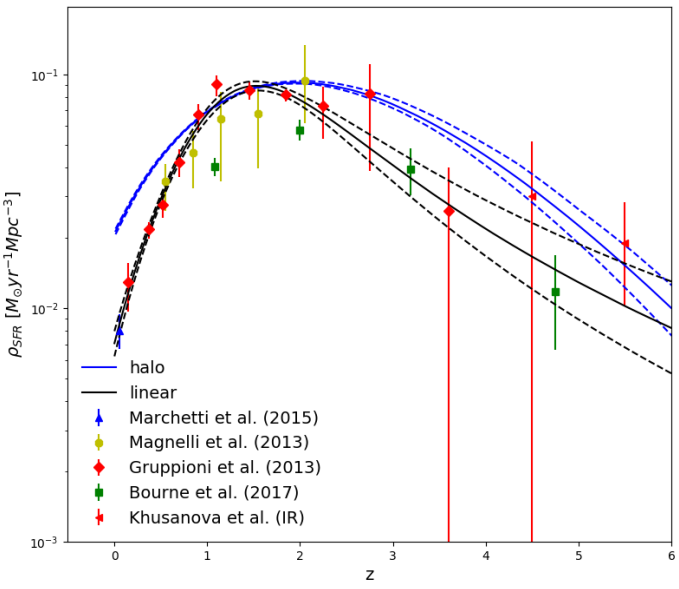

Fig. A.1. Measurements of the SFRD using galaxy surveys (Madau & Dickinson, 2014). Black solid line shows the SFRD as measured by the CIB linear model of Maniyar et al. (2018). Blue solid line shows the corresponding constraints when the SFRD values from the galaxies are not considered as priors while performing the fit of the CIB halo model. The dotted black, and red lines show the 1σ regions.

Figure A.1 shows the results when these external measurements are not considered as priors while finding the best fit parameters of the CIB model. Although we are able to fit the CIB power spectra with these parameters, it is evident that they predict excessive SFRD at, at least low redshifts. Thus, it is quite important to include these measurements as priors in our model.

Appendix B: Alternate parameterizations

Apart from the lognormal parameterization considered for η, we studied several different parameterizations. One of them was inspired by the approach taken by Moster et al. (2013) where they connect the galaxy mass with the corresponding host halo mass through a double power law parameterization. For our case, we used a double power law to describe the relation between η and M_h which goes as

$$\frac{\mathrm{SFR}}{\mathrm{BAR}} = \eta = \eta_{\mathrm{max}}\Big[\Big(\frac{M_h}{M_{\mathrm{max}}}\Big)^{-\beta} + \Big(\frac{M_h}{M_{\mathrm{max}}}\Big)^{\gamma}\Big]^{-1}, \tag{B.1}$$

where β, and γ describe the η at low mass and high mass end respectively. These two parameters allow us to have asymmetrical distribution around the mass of maximum efficiency. We fit this parameterization with all the data sets and external constraints as mentioned in Sect. 3. It was found that the data used are not sensitive and thus cannot constrain the low mass end slope β. Therefore, we fixed the value of β and let γ evolve with redshift (for $z \leq 1.5$) to avoid very massive halos contributing significantly to the SFR at low redshift in line with the reasoning presented in Sec. 2.1. Although this parameterization gave a good fit to the data (even better than the fiducial model using lognormal) and was able to produce a decent SFRD history, there was an unrealistically low contribution from the halos above the mass of maximum efficiency at high redshift. Therefore, even though this parameterization provided a better fit to the data than the fiducial model, we went along with the lognormal as the results were more physical.

Appendix C: Comparison of the Planck and Herschel CIB power spectra

Here we show some figures and plots comparing the measurements of the CIB power spectra from Planck and Herschel as well as the best fit values for the halo model obtained under different conditions. The shot noise values provided here have to be multiplied with the corresponding colour corrections at each frequency to obtain them in the νI_ν = constant convention.

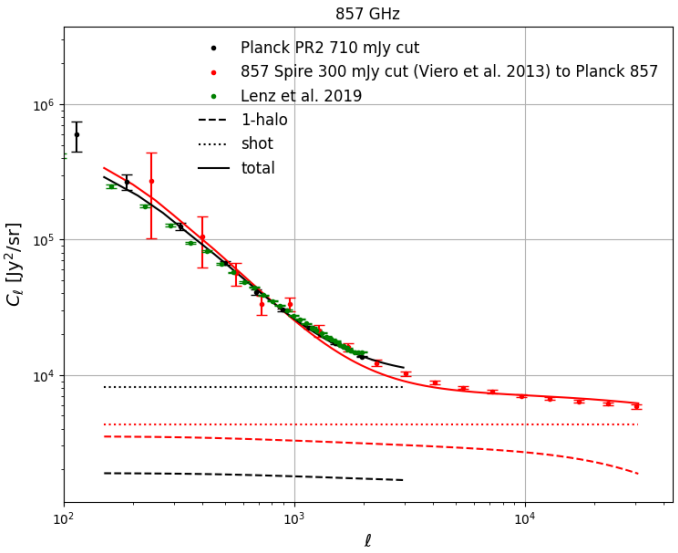

Fig. C.1. Measurements of the CIB power spectra from Planck Collaboration et al. (2014c), Viero et al. (2013a), and Lenz et al. (2019). Best fit models shown in this figure are obtained when fitting separately Planck and Herschel data. The Spire data have been rescaled to Planck data using the cross-calibration factor derived in Bertincourt et al. (2016) and the factor that allows to convert the measurement through the Spire bandpass into a measurement as it would be obtained through the Planck bandpass from Lagache et al. (2019). Overall, $C_\ell^{\mathrm{Planck,857GHz}} = 1.008 \times C_\ell^{\mathrm{Spire,857GHz}}$.

Halo model parameters	$\eta_{\rm max}$	$\log_{10} M_{\rm max}$	$\sigma_{M_{h0}}$	τ
$z_c = 1.5$ (fixed)	$0.52^{+0.03}_{-0.02}$	$12.73^{+0.02}_{-0.02}\ M_\odot$	$1.24^{+0.12}_{-0.13}$	$0.82^{+0.09}_{-0.09}$
HFI shot noise	$\mathrm{SN}^{\rm pl}_{217}$	$\mathrm{SN}^{\rm pl}_{353}$	$\mathrm{SN}^{\rm pl}_{545}$	$\mathrm{SN}^{\rm pl}_{857}$
	$14^{+0.71}_{-0.71}$	$357^{+9.91}_{-8.66}$	$2349^{+37.11}_{-34.16}$	$7407^{+190.48}_{-179.71}$
HFI calibration	$f^{\rm cal}_{217}$	$f^{\rm cal}_{353}$	$f^{\rm cal}_{545}$	$f^{\rm cal}_{857}$
	$1.00^{+0.01}_{-0.01}$	$1.00^{+0.01}_{-0.01}$	$0.99^{+0.03}_{-0.03}$	$1.05^{+0.03}_{-0.03}$

Table C.1. Marginalised values of all the model parameters given at a 68 % confidence level when we fit only for the Planck data considering the $f^{\rm cal}_\nu$ parameters at all Planck frequency channels centered at one with error bars of 0.05. We get a χ^2 value of 85 for 80 data points.

Halo model parameters	$\eta_{\rm max}$	$\log_{10} M_{\rm max}$	$\sigma_{M_{h0}}$	τ
$z_c = 1.5$ (fixed)	$0.52^{+0.04}_{-0.04}$	$12.98^{+0.02}_{-0.02}\ M_\odot$	$1.41^{+0.11}_{-0.10}$	$0.94^{+0.07}_{-0.07}$
Spire shot noise	$\mathrm{SN}^{\rm sp}_{600}$	$\mathrm{SN}^{\rm sp}_{857}$	$\mathrm{SN}^{\rm sp}_{1200}$	
	$1876^{+62.56}_{-54.50}$	$4199^{+164.88}_{-148.09}$	$4602^{+399.66}_{329.33}$	
HFI/Spire cross-calibration	$f^{\rm cal}_{600}$	$f^{\rm cal}_{857}$	$f^{\rm cal}_{1200}$	
	$1.06^{+0.01}_{-0.01}$	$1.02^{+0.01}_{-0.01}$	$1.00^{+0.03}_{-0.03}$	

Table C.2. Marginalised values of all the model parameters given at a 68 % confidence level when we fit only for the Herschel data considering the $f^{\rm cal}_\nu$ parameters at all Herschel frequency channels as done in our original analysis. We get a χ^2 value of 221 for 102 data points.

Halo model parameters	$\eta_{\rm max}$	$\log_{10} M_{\rm max}$	$\sigma_{M_{h0}}$	τ
$z_c = 1.5$ (fixed)	$0.40^{+0.03}_{-0.02}$	$12.95^{+0.02}_{-0.02}\ M_\odot$	$1.87^{+0.12}_{-0.13}$	$1.42^{+0.10}_{-0.10}$
HFI shot noise	$\mathrm{SN}^{\rm pl}_{217}$	$\mathrm{SN}^{\rm pl}_{353}$	$\mathrm{SN}^{\rm pl}_{545}$	$\mathrm{SN}^{\rm pl}_{857}$
	$13^{+0.71}_{-0.71}$	$352^{+9.91}_{-8.66}$	$2021^{+37.11}_{-34.16}$	$7279^{+190.48}_{-179.71}$
Spire shot noise	$\mathrm{SN}^{\rm sp}_{600}$	$\mathrm{SN}^{\rm sp}_{857}$	$\mathrm{SN}^{\rm sp}_{1200}$	
	$1150^{+62.56}_{-54.50}$	$2528^{+164.88}_{-148.09}$	$4393^{+399.66}_{329.33}$	
HFI/Spire cross-calibration	$f^{\rm cal}_{600}$	$f^{\rm cal}_{857}$	$f^{\rm cal}_{1200}$	
	$1.24^{+0.01}_{-0.01}$	$1.19^{+0.01}_{-0.01}$	$1.04^{+0.03}_{-0.03}$	

Table C.3. Marginalised values of all the model parameters given at a 68 % confidence level when we fit for both the Planck and Herschel data considering the $f^{\rm cal}_\nu$ parameters at all Herschel frequency channels centered at one with error bars of 0.05. We get a χ^2 value of 105 for 80 Planck data points and 127 for 102 Herschel data points with unrealistically high $f^{\rm cal}_\nu$ values.

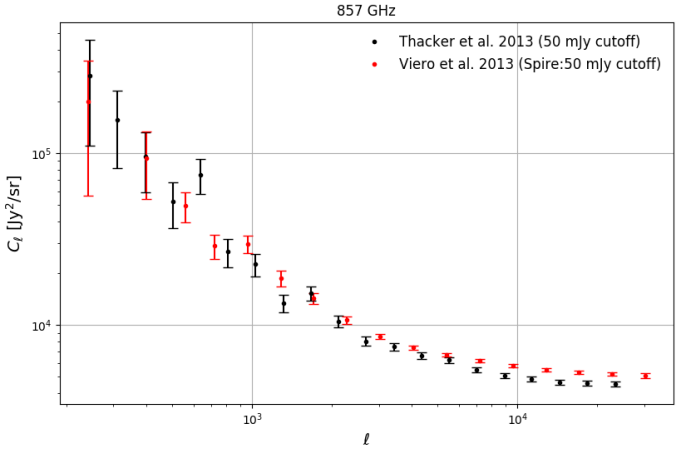

Fig. C.2. Measurements of the CIB power spectra from Thacker et al. (2013) and Viero et al. (2013a) for a flux cut of 50 mJy.

Halo model parameters	$\eta_{\rm max}$	$\log_{10} M_{\rm max}$	$\sigma_{M_{h0}}$	τ
$z_c = 1.5$ (fixed)	$0.43^{+0.04}_{-0.04}$	$12.95^{+0.02}_{-0.02}\ M_\odot$	$1.60^{+0.11}_{-0.10}$	$1.06^{+0.07}_{-0.07}$
Spire shot noise	$\mathrm{SN}^{\rm sp}_{600}$	$\mathrm{SN}^{\rm sp}_{857}$	$\mathrm{SN}^{\rm sp}_{1200}$	
	$1137^{+62.56}_{-54.50}$	$2502^{+164.88}_{-148.09}$	$4389^{+399.66}_{329.33}$	
Spire calibration	$f^{\rm cal}_{600}$	$f^{\rm cal}_{857}$	$f^{\rm cal}_{1200}$	
	$1.27^{+0.01}_{-0.01}$	$1.21^{+0.01}_{-0.01}$	$1.05^{+0.03}_{-0.03}$	

Table C.4. Marginalised values of all the model parameters given at a 68 % confidence level when we fit only for the Herschel data considering the $f_\nu^{\rm cal}$ parameters at all Herschel frequency channels centered at one with error bars of 0.05. We get a χ^2 value of 138 for 102 Herschel data points with unrealistically high $f_\nu^{\rm cal}$ values.

Halo model parameters	$\eta_{\rm max}$	$\log_{10} M_{\rm max}$	$\sigma_{M_{h0}}$	τ
$z_c = 1.5$ (fixed)	$0.52^{+0.09}_{-0.09}$	$12.86^{+0.02}_{-0.02}\ M_\odot$	$1.22^{+0.19}_{-0.16}$	$0.81^{+0.13}_{-0.11}$
Spire shot noise	$\mathrm{SN}^{\rm sp}_{600}$	$\mathrm{SN}^{\rm sp}_{857}$	$\mathrm{SN}^{\rm sp}_{1200}$	
	$3441^{+62.56}_{-54.50}$	$7204^{+164.88}_{-148.09}$	$8326^{+399.66}_{329.33}$	
Spire calibration	$f^{\rm cal}_{600}$	$f^{\rm cal}_{857}$	$f^{\rm cal}_{1200}$	
	$1.05^{+0.01}_{-0.01}$	$1.01^{+0.01}_{-0.01}$	$1.03^{+0.03}_{-0.03}$	

Table C.5. Marginalised values of all the model parameters given at a 68 % confidence level when we fit only for the Herschel data upto $\ell < 3000$ considering the $f_\nu^{\rm cal}$ parameters at all Herschel frequency channels as done in our original approach. We get a χ^2 value of 36 for 42 Herschel data points.

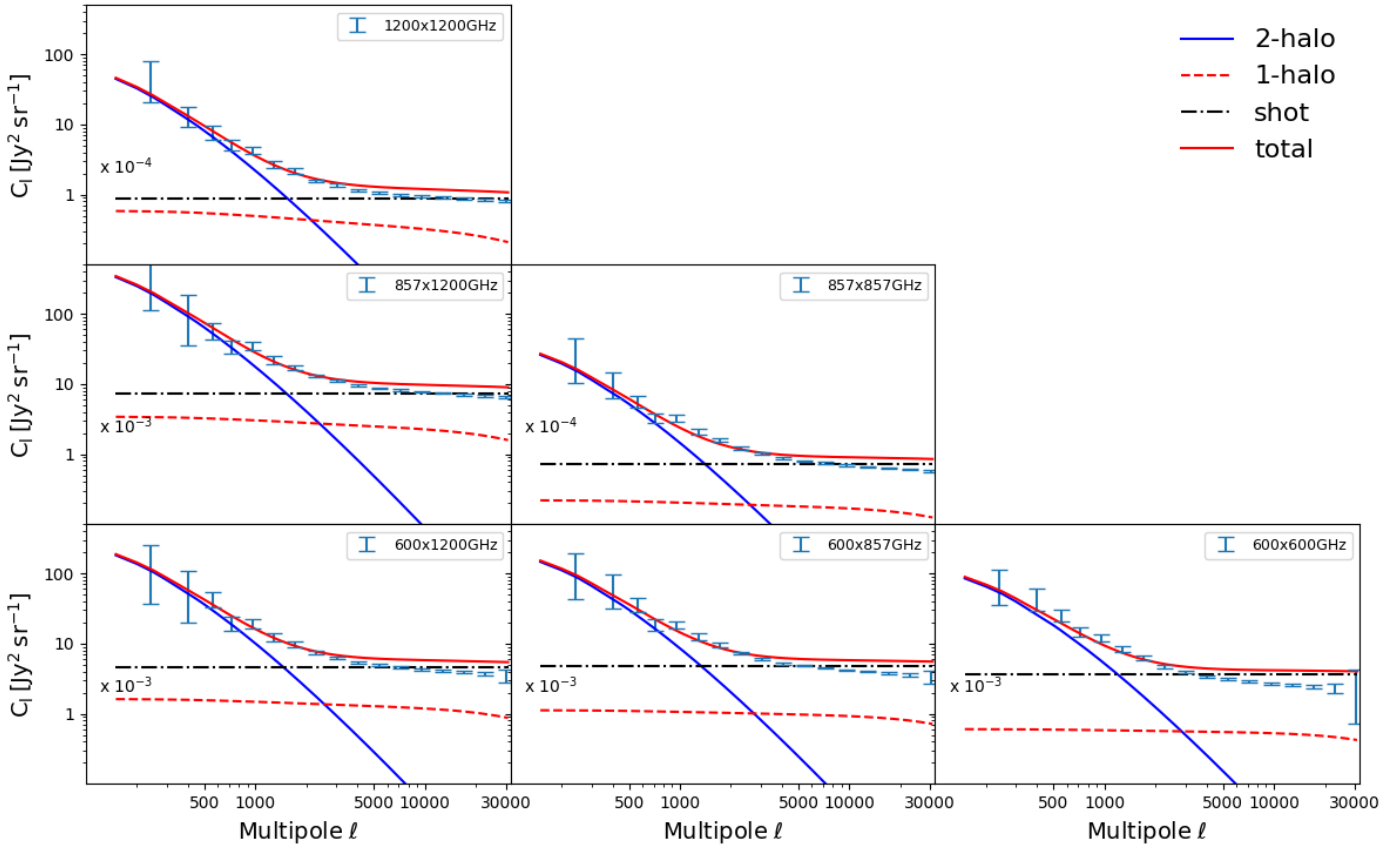

Fig. C.3. Measurements of the CIB auto- and cross-power spectra obtained by *Herschel*/SPIRE (Viero et al., 2013a) and the best fit CIB halo model with its different components when fitting *Herschel*/SPIRE data only for $\ell < 3000$.